iScience

CellPress
OPEN ACCESS

Article

Tumor Microenvironment-Activated Degradable Multifunctional Nanoreactor for Synergistic Cancer Therapy and Glucose SERS Feedback

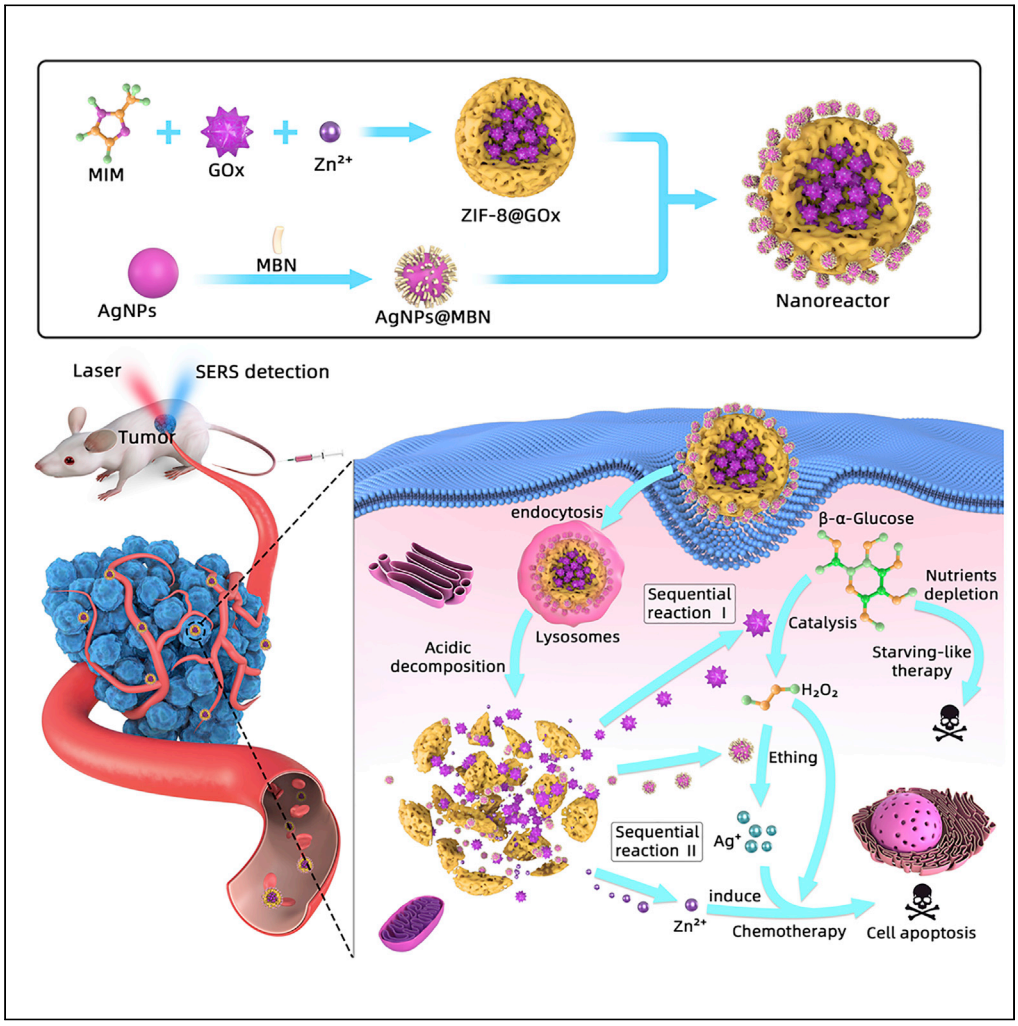

Dan Sun, Guohua Qi, Kongshuo Ma, Xiaozhang Qu, Weiqing Xu, Shuping Xu, Yongdong Jin

xusp@jlu.edu.cn (S.X.)
ydjin@ciac.ac.cn (Y.J.)

HIGHLIGHTS

This nanoreactor integrates *in vivo* sensing and synergistic therapy capabilities

The ZIF-8 nanocarrier protects GOx from deactivation and immune clearance

The nanoreactor is biodegradable, avoiding the side effects on tumor-bearing mice

Instant non-invasive glucose feedback capability realized by *in vivo* SERS

Sun et al., iScience *23*, 101274
July 24, 2020
https://doi.org/10.1016/j.isci.2020.101274

iScience

CellPress
OPEN ACCESS

Article

Tumor Microenvironment-Activated Degradable Multifunctional Nanoreactor for Synergistic Cancer Therapy and Glucose SERS Feedback

Dan Sun,[1,4] Guohua Qi,[2,4] Kongshuo Ma,[2,3] Xiaozhang Qu,[1] Weiqing Xu,[1] Shuping Xu,[1,5,*] and Yongdong Jin[2,3,*]

SUMMARY

Integration of disease diagnosis and therapy *in vivo* by nanotechnology is a challenge in the design of multifunctional nanocarriers. Herein, we report an intelligent and degradable nanoreactor, an assembly of the 4-mercaptobenzonitrile-decorated silver nanoparticles (AgNPs@MBN) and the glucose oxidase (GOx)-loaded metal-organic-framework (ZIF-8@GOx), which can be activated by tumor microenvironment to start the catalytic cascade-enhanced chemo-starvation synergistic therapy and simultaneous self-sense of cellular glucose level. Under the mild acidic microenvironment of tumor, the nanoreactor will collapse to release GOx that triggers a catalytic cascade reaction *in vivo*, depleting glucose, etching AgNPs@MBN, and producing toxic H_2O_2, Ag^+, and Zn^{2+} ions, all of which work together to inhibit tumor growth. The AgNPs@MBN as SERS nanoprobe reads out glucose concentration noninvasively in tumor to achieve instant feedback of therapeutic progression. This work proposes a promising example of using enzyme-encapsulated biomineralized MOFs as an effective anticarcinogen for clinical applications.

INTRODUCTION

Cancer remains a major threat to human health. To combat it, a variety of cancer therapeutic approaches have been developed (Lin et al., 2018; Yang et al., 2019; 2019b,) and widely employed in the clinic including surgery, chemotherapy, and ultrasound, photodynamic, photothermal, and radiotherapy. However, these strategies may cause severe damages to the surrounding normal tissues (Cheng et al., 2014; Liang et al., 2019) and/or induce undesired tumor metastasis (Song et al., 2016; Zhang et al., 2015). Therefore, minimally invasive or noninvasive precise therapeutic modalities, with high spatial/temporal controllability and less toxicity to healthy tissues, are still highly desired (Li et al., 2014; Ge et al., 2014; Han et al., 2018; Kotagiri et al., 2015).

Recently, glucose oxidase (GOx)-based cancer starvation therapy that depletes glucose and engenders toxic H_2O_2/gluconic acid in the presence of oxygen has been explored (Chang et al., 2017; Wang et al., 2016; Zhang et al., 2018a) as a targeting therapeutic strategy for cancers due to its powerful ability to change tumor microenvironments. Moreover, the generated H_2O_2 not only markedly enhances tumor oxidative stress but also can be converted into ·OH radicals to kill cancer cells (Wang et al., 2019b). Thus this strategy can be further integrated with other therapeutic methods to achieve enhanced synergistic therapeutic effects (Wang et al., 2019c; Ma et al., 2019; Tang et al., 2019). The naked GOx exposed in biological environments is particularly prone to inactivation. Also, it has the weaknesses of short *in vivo* half-life, immunogenicity, and systematic toxicity (Fu et al., 2018). Thus, nanocarriers (inorganic or organic) for GOx (Wang et al., 2016; Zhang et al., 2018a) are highly suggested in many GOx-based starvation therapeutic strategies. However, these nanocarriers are usually undegradable *in vivo*, and hence may cause biotoxicity. Therefore, a degradable and intelligent nanocarrier for precise GOx-based starvation therapy is urgently desired.

Metal-organic frameworks (MOFs) are a class of highly crystalline, porous, and degradable solid-state materials constructed by metal ions and organic linkers (Wang et al., 2019a; Schoedel et al., 2016). It affords a promising biomedical nanocarrier platform for encapsulating drugs, antibodies, genes, enzymes, etc. (Feng et al., 2018; Chen et al., 2019) for *in vivo* drug delivery. These MOF cages can protect proteins from the attack of proteases and the clearance of the mononuclear phagocyte system in physiological environments (Cheng et al., 2019; Gao et al., 2019; Lin et al., 2019; Zhang et al., 2018b). Recent reports showed

[1]State Key Laboratory of Supramolecular Structure and Materials, Institute of Theoretical Chemistry, College of Chemistry, Jilin University, 2699 Qianjin Avenue, Changchun 130012, P. R. China

[2]State Key Laboratory of Electroanalytical Chemistry, Changchun Institute of Applied Chemistry, Chinese Academy of Sciences, Changchun, Jilin 130022, P. R. China

[3]University of Science and Technology of China, Hefei 230026, P. R. China

[4]These authors contributed equally

[5]Lead Contact

*Correspondence: xusp@jlu.edu.cn (S.X.), ydjin@ciac.ac.cn (Y.J.)

https://doi.org/10.1016/j.isci.2020.101274

that some of them could react with the cellular microenvironments of cancers, e.g., ZIF-8 and UiO-66 for pH, ZIF-90 for ATP (Cai et al., 2019). These intelligent responses of the MOF-based nanocarriers endow them with microenvironment-switchable drug-releasing ability, achieving effective tumor-targeted killing.

In this study, we developed a biomimetic, degradable, and intelligent nanoreactor (ZIF-8@GOx-AgNPs@MBN) for the catalytic cascade-enhanced chemo-starvation synergistic therapy of tumor. The nanoreactor was fabricated by the electrostatic assembly of the surface-enhanced Raman scattering (SERS) nanoprobes (AgNPs@MBN) on the GOx-encapsulated ZIF-8 MOF nanoparticle (ZIF-8@GOx). After the internalization of the nanoreactors by cancer cells, the GOx encapsulated in MOF can be gradually released according to the intercellular microenvironment of cancerous cells, to trigger a catalytic cascade reaction that can collapse the ZIF-8 cage, consume glucose, etch the AgNPs@MBN, and produce toxic H_2O_2, Zn^{2+}, and Ag^{+} ions, realizing the chemo-starvation synergistic therapy of cancer cells. Many studies have proved that Ag^{+} and Zn^{2+} ions have cytotoxicity on various cancer cell lines through the induction of oxidative stress, mitochondrial damage, autophagy, and cell apoptosis (Soenen et al., 2015; Skulachev et al., 1967; Manev et al., 1997; Link and Jagow, 1995; Gazaryan et al., 2007). And the nanoreactor can be gradually degraded in the lysosomes due to the mild acidic environment of lysosomes of cancer cells. Moreover, the SERS nanoprobes loaded on the nanoreactors can self-sense and provide a feedback of the glucose level simultaneously during the therapeutic progress due to the decreasing SERS intensity of the Raman reporter (MBN) caused by the H_2O_2-etching effect on AgNPs. We applied the nanoreactor for the treatment of cervical carcinoma cells (HeLa) and mice planted with the cervical carcinoma tumors. The chemo-starvation synergistic therapeutic effect of the nanoreactor for tumors was assessed, and the systemic toxicity was also evaluated. The merits of the designer multifunctional nanoreactor are obvious. (1) It integrates *in vivo* sensing and chemo-starvation synergistic therapy capabilities. (2) As the main element of the nanoreactor, the ZIF-8 nanocarrier protects GOx from deactivation and immune clearance. More importantly, it has an intelligent acid response to the tumor microenvironment, and its fragmentation triggers on-demand drug (GOx) release, which is a key step for the cancer-specific therapy. (3) The nanoreactor is biodegradable, avoiding the long-term accumulation of the nanomaterials and the side effects on tumor-bearing mice. (4) The nanoreactor has instant non-invasive glucose feedback capability for therapeutic effectiveness evaluation, realized by *in vivo* SERS. (5) The high payloads of GOx and SERS nanoprobes improve the therapeutic effect and strengthen the sensing ability.

RESULTS AND DISCUSSIONS

Characterization of ZIF-8@GOx-AgNPs@MBN

As displayed in Scheme 1, the hierarchical nanoreactor was constructed by the assembly of the AgNPs@MBN on the ZIF-8@GOx nanoparticle. Figures 1A–1D show the transmission electron microscopic (TEM) images of the components and the resulting nanoreactors. AgNPs with a diameter of ~13 $\pm$ 2.4 nm (Figure 1A and S1) were used for constructing the SERS nanoprobe, and our SERS measurements indicate that such a size of AgNPs affords acceptable SERS intensity for the Raman reporter MBN (Figure S2C). We chose MBN as the reporter because it has a unique band in the silent range of bio tissues, minimizing the interference of the living body during *in vivo* SERS detections The successful preparation of the AgNPs@MBN was evidenced by the UV-visible (UV-vis) spectra and zeta potential characterizations. The plasmonic band of AgNPs centered at 400 nm (Figure 1F) has a red shift after the MBN coating, whereas the zeta potential of the NPs also switches from −33.56 to −28.83 mV after the coating (Figure 1G).

The ZIF-8@GOx was prepared by the crystallization of the ZIF-8 precursors (zinc nitrate and 2-methylimidazole) with GOx under stirring. The average size distribution of the pure ZIF-8 is about 84 $\pm$ 4.3 nm (Figure 1B). The encapsulation of GOx in ZIF-8 NPs (ZIF-8@GOx) caused a size increase to 99 $\pm$ 6.9 nm (Figure 1C), ascribing to a promoted growth kinetics mediated by the GOx-seeded clusters. The zeta potential of the resulting ZIF-8@GOx is 28.6 mV, which is ~4 mV higher than that of pure ZIF-8 (24.4 mV, Figure 1G). Figure 1H shows the nitrogen adsorption analysis of the ZIF-8@GOx, manifested as Type 1 in shape. The Brunauer-Emmett-Teller analysis exhibits that the ZIF-8@GOx has a surface area of 841.27 m^2/g, which is smaller than that of the pure ZIF-8 NPs (1,014.36 m^2/g). The loading ratio of GOx in ZIF-8@GOx analyzed by thermogravimetric analysis was ~55 wt % (Figure S4). Moreover, the X-ray diffraction data confirm that ZIF-8@GOx maintains the same crystalline form as the pure ZIF-8 NPs (Figure S2B), suggesting that the doping of GOx does not alter the crystalline structure of ZIF-8.

Figure 1D shows the TEM image of the obtained nanoreactor. It can be observed that the AgNPs@MBN are randomly attached to the ZIF-8@GOx surface. The existence and uniform distributions of C, N, O, Zn, and

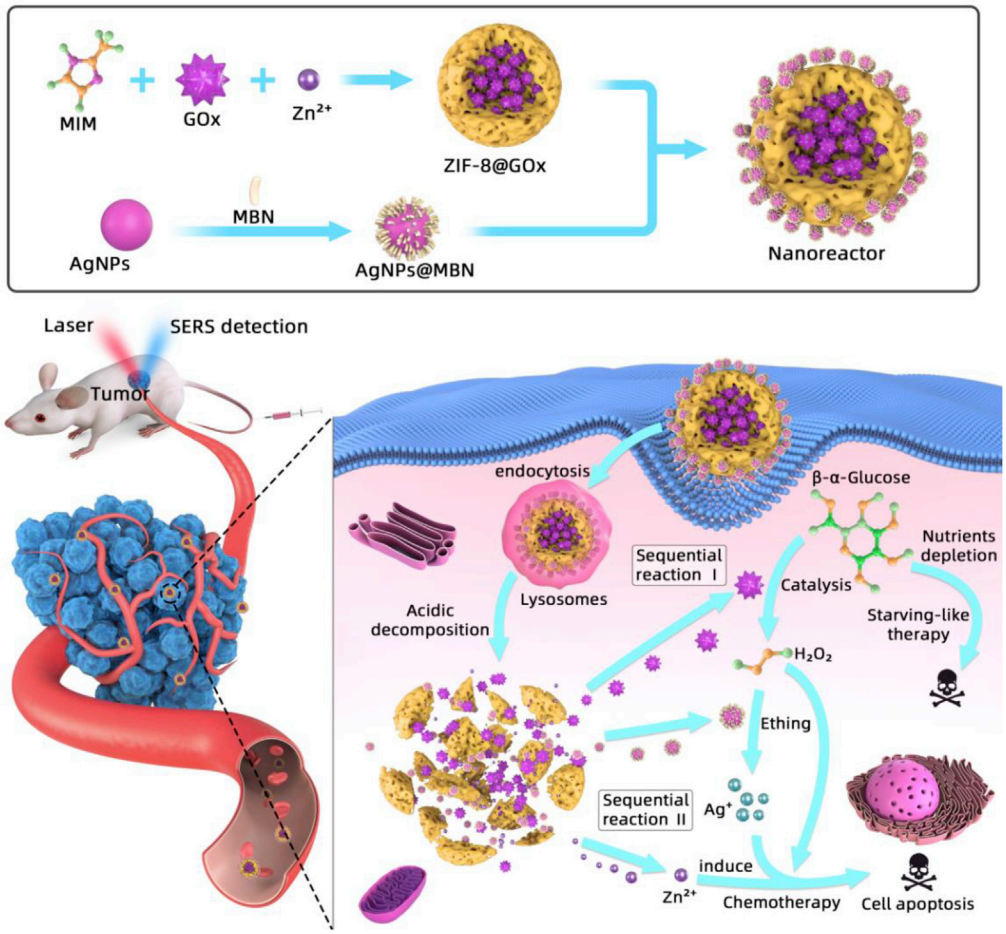

Scheme1. The Design of the Nanoreactor and Its Catalytic Cascade-enhanced Synergistic Chemo-Starvation Therapy for Cancer Cells

Ag were revealed by both elemental mapping (Figure 1E) and X-ray photoelectron spectroscopic analysis (Figure S3), affirming the successful assembly of the nanoreactors. The UV-vis spectrum of the ZIF-8@GOx-AgNPs@MBN shows a band at ~ 402 nm, which is mainly originated from the plasmon band of AgNPs (from AgNPs@MBN). The resulting nanoreactor gives a surface potential at 4.82 mV, which differs from either AgNPs@MBN (−28.83 mV) or ZIF-8@GOx (28.6 mV). The aforementioned data further verified the successful decoration of the AgNPs@MBN on the ZIF-8@GOx.

Tumor Microenvironment-Responsive Catalytic Cascade Reaction of the Nanoreactor

Owing to the acidic degradable feature of ZIF-8, the tailor-made nanoreactor could trigger a catalytic cascade reaction in an acidic tumor microenvironment, which can be employed to perform the synergistic tumor therapy based on the fast glucose metabolism and consumption of cancer cells (Hsu and Sabatini, 2008; Ying et al., 2012; Huo et al., 2017; Qi et al., 2018) and the poisoning of released metal ions (Scheme 1). Since the pH of the subcellular organelles in the cancer cells is more acidic as compared to that in the normal cells (Shen et al., 2018; Qi et al., 2019), the nanosensor starts degradation under an acidic environment within lysosomes of cancer cells; the fracture of the ZIF-8 skeleton structure produces zinc (Zn^{2+}) and releases the loaded GOx as well. So, this synergistic therapy is tumor cell selective and normal cell ineffective, realizing the targeting and selective therapy.

Although Zn^{2+} is an essential element for humans (Gao et al., 2017), it has toxic effects on mammalian cells at elevated concentrations as the elevation of Zn^{2+} can trigger the breakdown of the mitochondrial membrane potential, caspase activation, and cell apoptosis (Skulachev et al., 1967; Manev et al., 1997;

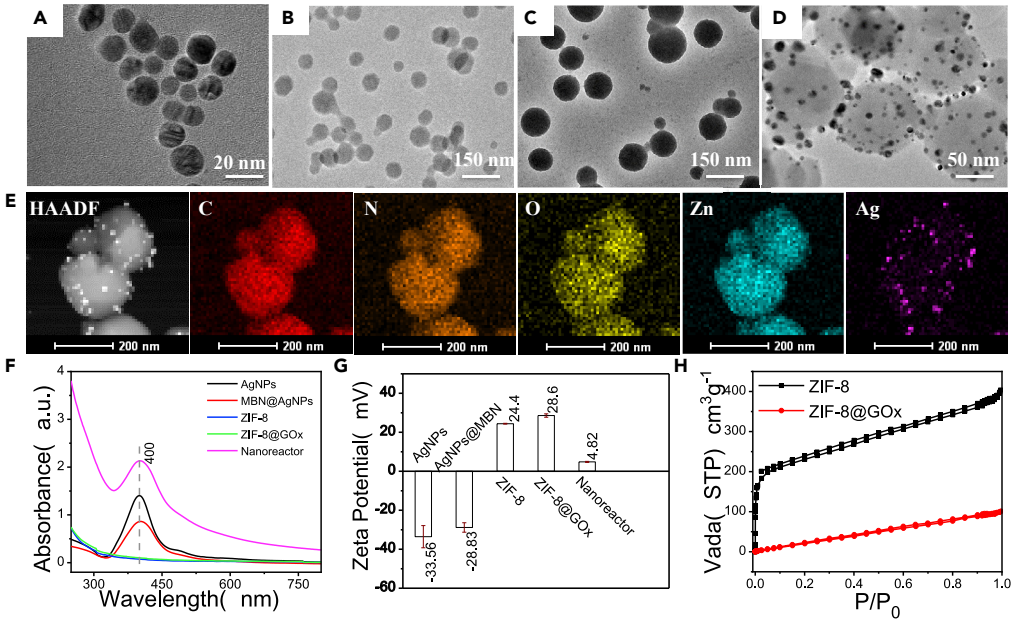

Figure 1. Characterization of Nanoreactors

(A–D) Typical TEM images of (A) AgNPs, (B) ZIF-8, (C) ZIF-8@GOx, and (D) the resulting ZIF-8@GOx-AgNPs@MBN nanoreactors.

(E) High-angle annular dark-field-scanning transmission electron microscopic and elemental mapping of the ZIF-8@GOx-AgNPs@MBN for C, N, O, Zn, and Ag.

(F and G) (F) The UV-vis absorption spectra and (G) zeta potentials of the AgNPs, AgNPs@MBN, ZIF-8, ZIF-8@GOx, and ZIF-8@GOx-AgNPs@MBN.

(H) Nitrogen adsorption analysis isotherms of ZIF-8 and ZIF-8@GOx.

Link and Jagow, 1995; Gazaryan et al., 2007). Moreover, the content of glucose in the cancerous cells is more than in normal cells (Huo et al., 2017; Chen et al., 2015), so that the exposed GOx could effectively deplete the glucose in cancerous cells, producing H_2O_2 that subsequently etches AgNPs into toxic Ag^+. Therefore, the deleterious substances (H_2O_2, Zn^{2+}, and Ag^+) produced by this catalytic cascade reaction of the nanoreactor, together with the starvation effect, will cooperatively kill tumor cells. Also, this synergistic therapy is selective for tumors due to the difference in the pH microenvironments between cancer and normal cells.

Equally importantly, in addition to the synergistic therapy capability, the designed nanoreactor also has the capability of glucose self-sensing, which is vital not only for the feedback of the intracellular glucose environment but also for the assessment of GOx activity of the nanoreactor. The sensing performance of the nanoreactor was assessed by using the SERS spectroscopy based on a "turn-off" mechanism (intensity decrease) of the Raman reporter (MBN) induced by the H_2O_2 etching effect on the AgNPs (described as Equations 1 and 2), in which the enzymatically produced H_2O_2 is glucose relevant.

$$D-\text{glucose} + O_2 + H_2O \xrightarrow{GOx} D-\text{gluconic acid} + H_2O_2 \quad \text{(Equation 1)}$$

$$2Ag + H_2O_2 + 2H^+ \rightarrow 2Ag^+ + 2H_2O \quad \text{(Equation 2)}$$

Clearly and as confirmed experimentally, only in the presence of glucose and acidic conditions, the SERS intensity of MBN was reduced (Figure 2A), proving enzymatic activity of GOx and degradability of the nanoreactor in an acidic environment.

ZIF-8 is considered as a good delivery carrier for enzyme, antibody, gene, and so on. ZIF-8 can protect these biomolecules from inactivity and immune clearance and maintain their biological function, which is key role for a nanocarrier (Lin et al., 2019; Zhang et al., 2018a, 2018b; Chen et al., 2018). In the present design, ZIF-8 is an acid-responsive material, and its drug release condition is proved to be 4.5 (Figure 2A). One concern is whether the enzymatic activity of GOx under acidic condition would be affected. To test

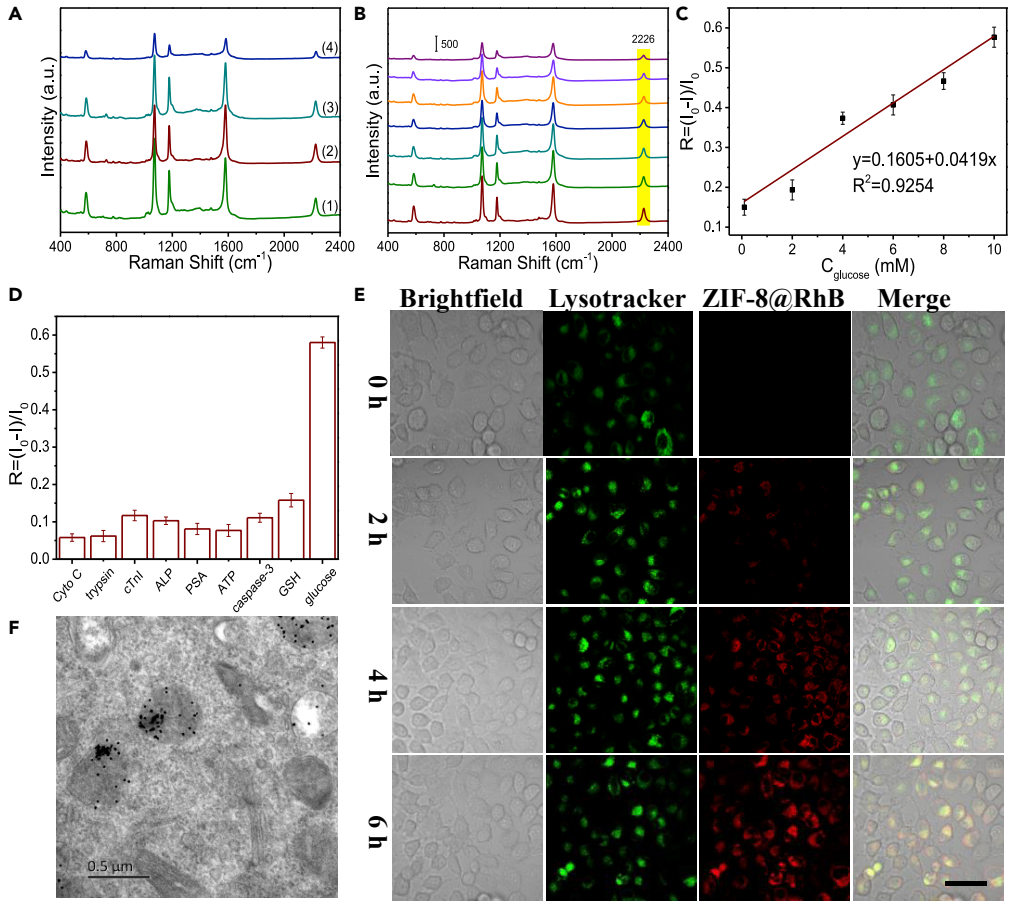

Figure 2. Tumor Microenvironment-Responsive Catalytic Cascade Reaction of the Nanoreactors

(A) SERS spectra of the ZIF-8@GOx-AgNPs@MBN nanoreactors without (1 and 3) or with 5 mM glucose (2 and 4) at pH = 7.0 (1 and 2) and pH = 4.5 (3 and 4).

(B) SERS spectra of the nanoreactors reacted with different concentrations of glucose (bottom to top: 0–10 mM) for 3 h at pH = 4.5.

(C) The plot of the SERS peak intensity with the concentrations of glucose.

(D) The selectivity of the nanoreactors for glucose over other negative controls according to the SERS intensity of 4-MBN at 2,226 cm^{-1}. The error bars are calculated from three trials.

(E) Fluorescence colocalization images of HeLa cells after incubation with the rhodamine B(RhB)-labeled (BSA)-encapsulated ZIF-8 NPs (red, ZIF-8@RhB) for different incubation times, while the lysosomes were stained with LysoTracker (green). Scale bar, 50 μm.

(F) Bio-TEM images of HeLa cells after incubation with the ZIF-8@GOx-AgNPs@MBN for 6 h.

this, a chromogenic reaction of tetramethyl benzidine (TMB) was conducted. In this sensing process, the hydroxyl radicals produced from the disproportionation of the enzymatically produced H_2O_2 under catalysis by horseradish peroxidase will oxidize colorless TMB to chromogenic TMB cation-free radicals, which can be assayed at 650 nm with a UV-vis spectrometer. The results (Figures S5A and S5B) indicate that the GOx maintained its good catalytic activity irrespective of whether they were encapsulated into ZIF-8 or were under acidic condition (pH = 4.5) (Figures S5C and S5D). In addition, the optimum pH for GOx activity is ~4 *in vitro* and the activity of GOx is about 616.6 U/mL in the acidic environment of the tumor (Figure S6). Fortunately, the activity of GOx is also not affected by the high temperature during the synthesis of the ZIF-8@GOx (Figure S7).

The AgNPs@MBN element on the nanoreactor shows a good linear response to the GOx/glucose reaction in a glucose concentration range of 0–10 mM (Figures 2B and 2C) with the lowest detectable concentration of 0.1 mM. This sensing shows high selectivity to glucose (Figure 2D) and fewer interferences from other substances in the biological environments.

Positioning of the Nanoreactor in Cells

The distribution of the nanoreactors within cells was disclosed by using confocal laser scanning microscopic imaging by using rhodamine B (RhB)-encapsulated ZIF-8 NPs (Figures S8 and 2E). From the fluorescence co-localization of the ZIF-8@RhB and the LysoTracker (green) in HeLa cells, we can observe that by increasing the culture time, more and more ZIF-8@RhB enters into cells, giving brighter red fluorescence; after 6-h cell incubation, the ZIF-8@RhB lights the whole cells and the cells still keep their morphology. The colocalization coefficient (Pearson's correlation coefficient) of the ZIF-8@RhB and the LysoTracker was calculated as 0.9914, indicating their high spatial consistency. Furthermore, the location of nanoreactors in the lysosomes was affirmed by bio-TEM (Figure 2F).

Therapeutic Effect of Nanoreactors for HeLa Cells

The treatment effect of the nanoreactors after being incubated with HeLa cells was then examined. The dose of the nanoreactor for cells was first evaluated. A safe concentration of the nanoreactor for HeLa cells for 24 h was optimized as less than 0.16 mg/mL by using MTT assay (Figure S9A). Figure 3A shows the fluorescence images of the live/dead cells stained by calcein-AM/propidium iodide after the cells were incubated with the nanoreactor (0.08 mg/mL) for different culture times. We can observe that ~95% cells are dead after incubation for 6 h and the percentage of the dead cells increases further with incubation time (Figure S9B). The therapeutic efficacy of the nanoreactors was further quantified by the flow cytometry experiments (the typical Annexin V-APC/7-AAD staining protocol, Figure 3B). The results were consistent with those of the aforementioned live/dead cell staining assay, indicating that HeLa cells died by the apoptotic pathway.

To confirm the synergy of multi-factors that drive cancerous cells to death, the cell viabilities of various forms of the nanocomposites including the control group (PBS), AgNPs@MBN, ZIF-8, ZIF-8@GOx, and ZIF-8@GOx-AgNPs@MBN, incubated with HeLa cells for 24 h, were comparatively examined via the standard MTT assay and the fluorescence live/dead cell staining as well. As clearly shown in Figures 3C and S9C, all the control groups show no significant cell damage. Comparatively, the cell viability rate of the nanoreactor group decreases to 5.97%, demonstrating the strong cell-killing ability of the nanoreactors. We also found experimentally that the same concentration of the nanoreactors (0.08 mg/mL) is non-toxic to the normal H8 cells (Figures S10A, S10B and S11), which confirms our expectation that the normal cells (H8 cell) with a higher pH microenvironment are hard to trigger the catalytic cascade reactions of the nanoreactors.

To check the synergistic effects of the H_2O_2, Ag^+, Zn^{2+}, and glucose consumption on cancerous cell killing, we first performed the glucose consumption test in HeLa cells after they were incubated with the nanoreactor for 6 h, by taking advantage of the glucose self-sensing capability of the nanoreactors. As seen from Figure 3D, the SERS intensity of MBN gradually weakened over time, indicating that intracellular glucose was gradually consumed to the starvation state. To testify the generation of hydrogen peroxide in the catalytic cascade reaction within HeLa cells, an H_2O_2 kit assay was used for the HeLa cells incubated with the nanoreactor. Figure S12 shows the fluorescence images of H_2O_2 within the tested HeLa cells after incubation with the nanoreactors for different time. The fluorescence intensity increased gradually, indicating that more and more H_2O_2 was generated in the catalytic cascade reactions. The toxicities of individual Ag^+ and Zn^{2+} to HeLa cells at different concentrations were further studied. The cell survival rate was ~70% when the concentration of Zn^{2+} is 100 μM (Figure 3E), whereas the same concentration of Ag^+ made the cell survival rate lower than ~25%, proving that Ag^+ has a higher toxicity than Zn^{2+} to tumor cells. The viabilities of HeLa cells treated with the two kinds of metal ions (Ag^+ and Zn^{2+}) under the different concentrations with or without glucose were also tested by the MTT assay (Figure 3F). Compared with those in the presence of glucose, the tumor cells exhibited a starved stage when glucose has been removed from the culture medium, and lower concentrations of Ag^+/Zn^{2+} in the absence of glucose can kill more cancer cells (Figure 3F), confirming the enhanced synergistic therapeutic effect by combined treatment of starvation and the poisoning of metal ions.

In Vivo Tumor Therapy

Motivated by the outstanding biocompatibility and excellent therapeutic performance of the nanoreactor *in vitro*, we proceeded to assess its *in vivo* therapeutic behavior by examining the cervical tumor

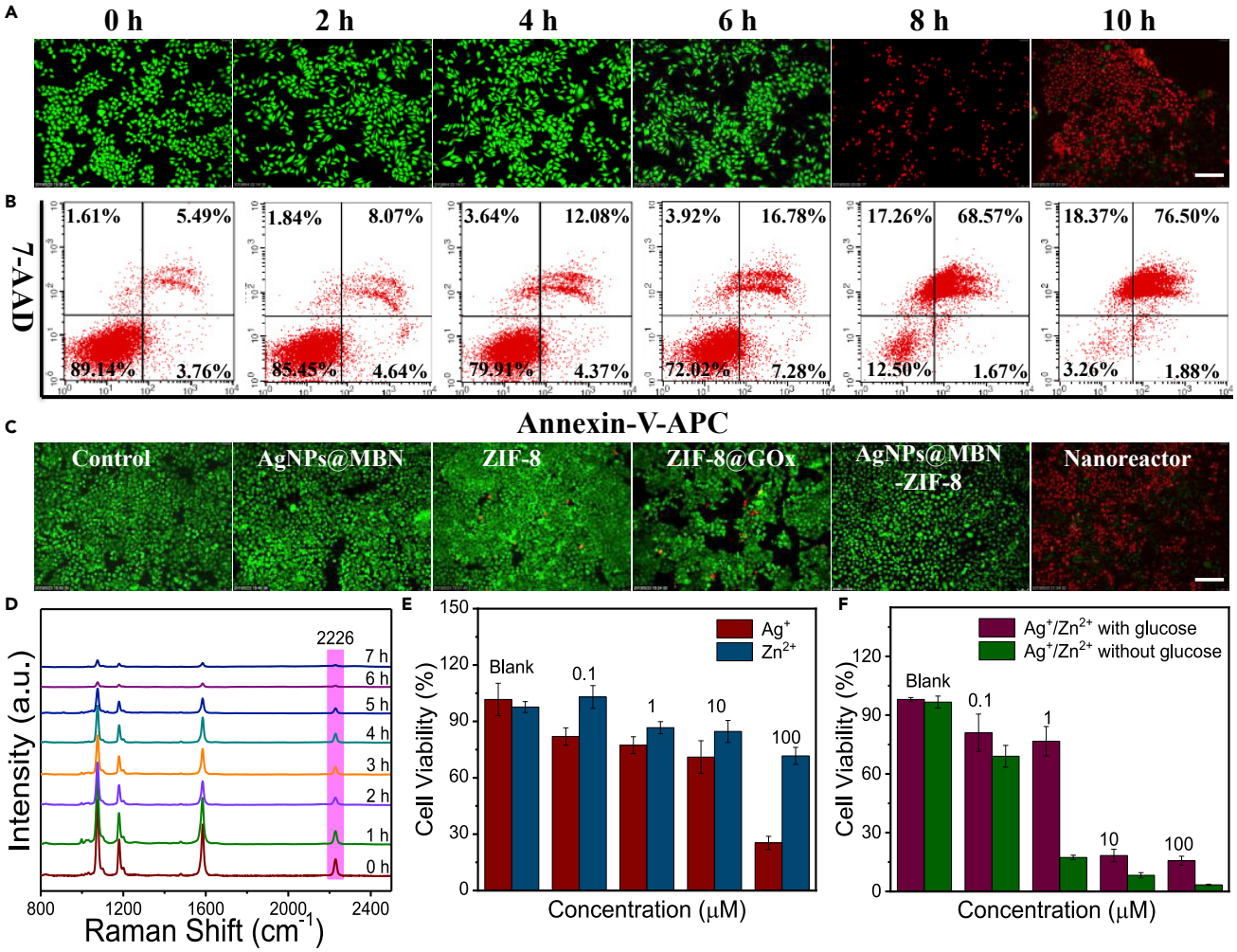

Figure 3. Therapeutic Effect of Nanoreactors for HeLa Cells

(A) Confocal fluorescent images of HeLa cells after incubation with ZIF-8@GOx-AgNPs@MBN at different times (n = 3). All scale bars, 80 μm.

(B) Flow apoptosis assay of HeLa cells after different treatment times (n = 3).

(C) The confocal fluorescent images of live and dead HeLa cells that underwent different treatments, including control (PBS), ZIF-8, ZIF-8@GOx, AgNPs@MBN, and ZIF-8@GOx-AgNPs@MBN. Cells were stained by Calcein-AM/propidium iodide, and the green and red colors stand for the alive and dead cells, respectively (n = 3). All scale bars, 80 μm.

(D) SERS spectra of HeLa cells incubated with ZIF-8@GOx-AgNPs@MBN for different times.

(E and F) Relative cell viabilities of HeLa cells incubated with different concentrations of Ag^{+}, Zn^{2+} (E), and Ag^{+}/Zn^{2+} with or without glucose for 24 h (F), determined by the MTT assay.

xenografted on the specific pathogen-free BALB/c nude mice (Figure S13). The cervical tumor-bearing mice with initial tumor volumes of 200 mm^3 were randomly divided into the following six groups: treated by (1) PBS, (2) AgNPs@MBN, (3) ZIF-8@GOx, and (4–6) nanoreactors with different concentrations (50, 100, and 200 μg/mL, respectively). During a therapeutic period of 14 days, the body weights of mice in control and all therapeutic groups show no significant variations, which indicates that the nanoreactor provides excellent biocompatibility in the whole therapeutic process (Figure 4A). Compared with other groups, the nanoreactor (200 μg/mL) presents satisfactory suppression effects on the tumor (Figures 4B–4E). The suppression rate, in terms of the variation of the relative tumor volume (Figure 4G), was calculated as 96.8%, implying the excellent *in vivo* therapeutic performance of the nanoreactor.

The tumor tissues of mice in different groups after the treatment were collected and analyzed by hematoxylin and eosin (H&E) staining assays, and the results are presented in Figure 4F. In the AgNPs@MBN and the nanoreactor groups, the apparent deformation, shrinking of the nuclei, and destruction of the membrane

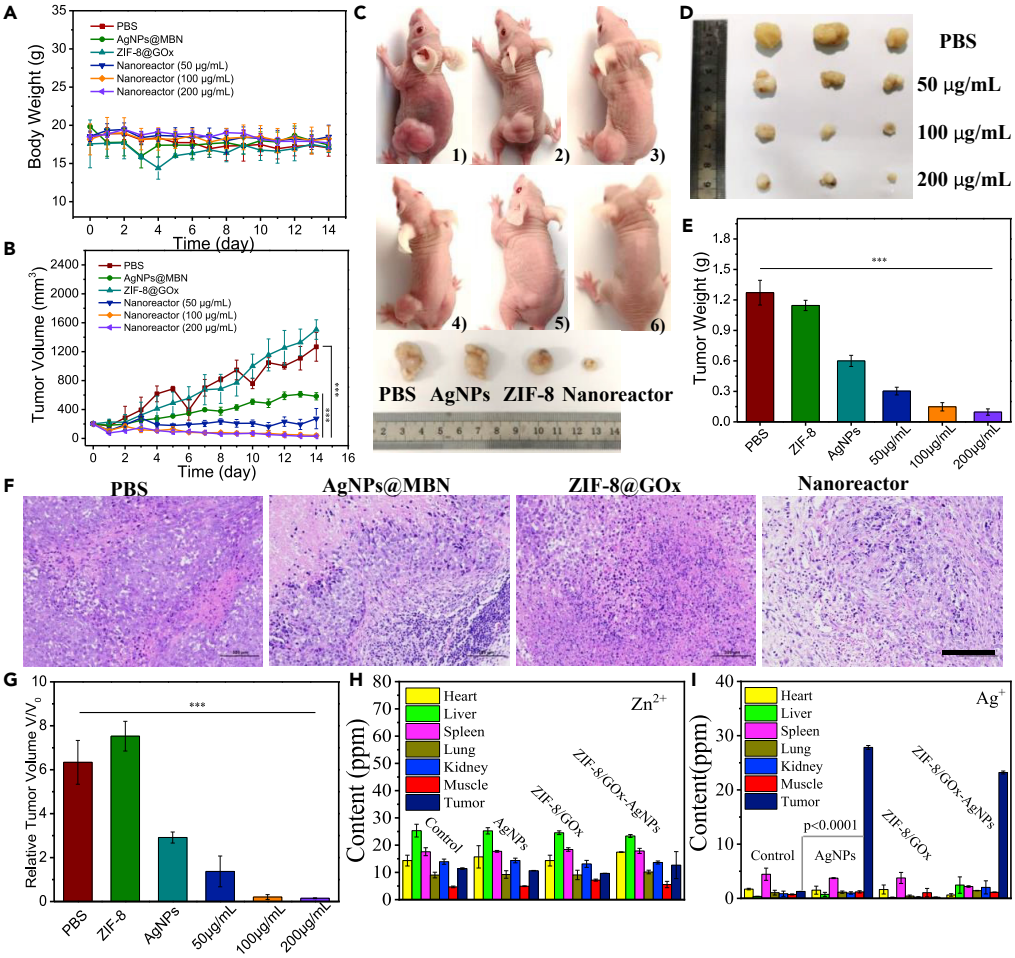

Figure 4. *In Vivo* Tumor Therapy and Biosafety of the Nanoreactors

(A and B) (A) The body weight changes and tumor volume curve (B) of HeLa tumor-bearing mice in each group, which underwent various treatments including AgNPs@MBN, ZIF-8@GOx, and ZIF-8@GOx-AgNPs@MBN at different concentrations (50, 100, and 200 μg/mL), recorded every day.

(C–E) (C) Representative digital photographs of the tumor-bearing mice after different therapies for 14 days. 1–6: PBS, AgNPs@MBN, ZIF-8@GOx, and ZIF-8@GOx-AgNPs@MBN at different concentrations (50, 100, and 200 μg/mL). The photographs (D) and weights (E) of the tumors in each group were collected on day 14.

(F) H&E staining of the tumor slides after the different treatments. All scale bars, 25 μm.

(G–I) (G) The relative tumor volume 14 d after treatment at different conditions. The biodistribution of Zn^{2+} (H) and Ag^{+} (I) in main tissues and tumors in 48 h of intravenous administrations of the ZIF-8@GOx-MBN@AgNPs.

p values in (B, E, and G) were calculated by the t test, where ***$p < 0.001$ indicate that the two being compared have a very high degree of discrimination.

integrity were all observed, indicating severe damage to tumor cells. For tumors in other groups, we observed no distinct injury.

Biosafety of the Nanoreactors

To evaluate the biosafety of the nanoreactors, the biodistributions of silver and zinc elements in the main organs and tumors were determined using the inductively coupled plasma mass spectrometry (ICP-MS). As shown in Figures 4H, 4I, and S15, the silver element was observed mainly accumulated in the tumor, without serious side effects on other organs (heart, liver, spleen, lung, kidney, and muscle), whereas the contents of the zinc element were almost unchanged in all tested organs and tumors. The histopathological evaluation of these major organs and the hematology-related assays were further carried out after the treatment. As shown in Figure S14, the major organs stained by H&E show no significant pathological changes between the control groups and the treatment groups.

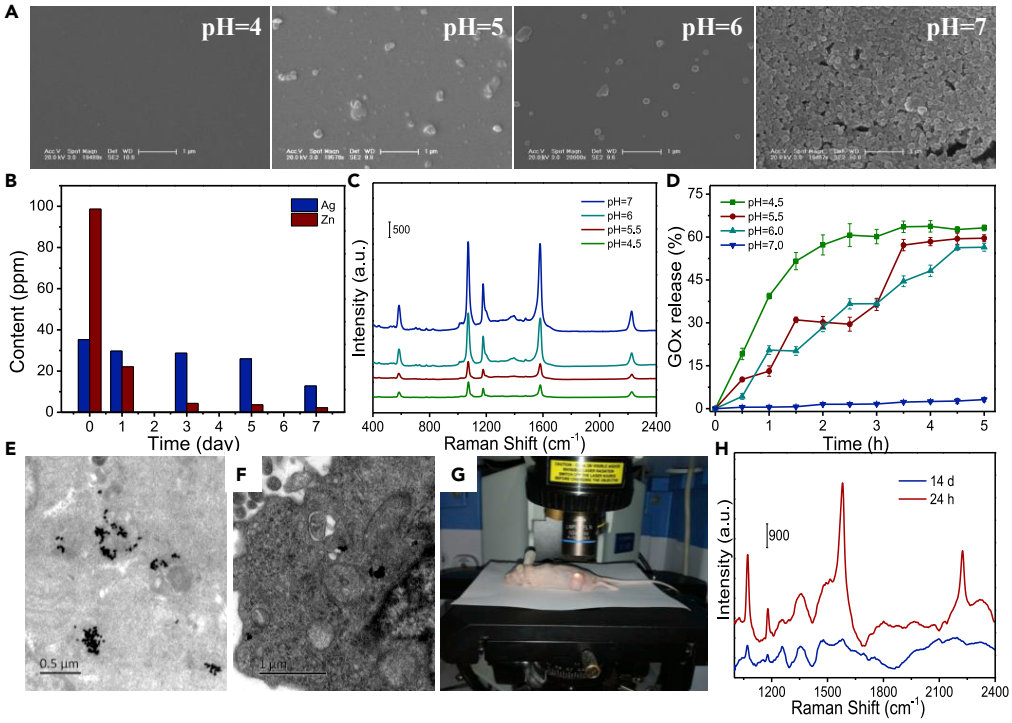

Figure 5. Biodegradability of the Nanoreactors

(A) Scanning electron microscopic images of the nanoreactors under different pH values.

(B) The biodistribution of Zn^{2+} and Ag^{+} in the extracted lysosomes of HeLa cells with treatment time, assessed by ICP-MS.

(C) SERS spectra of the nanoreactor after reacting with 5.0 mM glucose for 3 h at different pH values.

(D) GOx release from the nanoreactors, measured by SERS method.

Bio-TEM images of the tumor tissues 6 h postinjection of the nanoreactor (E) or 14 days after treatment with this nanoreactor (F).

(G) Photograph shows *in situ* SERS measurements of a mouse by a confocal Raman microspectrometer. A laser beam is focusing on the tumor.

(H) SERS spectra recorded from the tumor site of a mouse with intravenous preinjection of the nanoreactor for 24 h and 14 days, respectively.

The blood chemistry analyses were also conducted by checking standard eight hematological biomarkers (Figure S16). The results manifest no distinct abnormality in blood chemistry before and after treatment for 14 days, indicating negligible side effects of the nanoreactor. In addition, analyses of the microelements within blood show that the zinc element has no abnormal change between the control groups and treatment groups (Table S1). These results demonstrate that this intelligent nanoreactor not only can effectively suppress tumor growth but also displays satisfactory low toxicity.

Biodegradability of the Nanoreactors

Biodegradation of the nanoreactors was evaluated under neutral (pH = 7.0) and acidic (pH = 4.0–6.0) media, which imitate the *in vivo* neutral healthy body fluids and intratumoral mildly acidic environment, respectively. As shown by scanning electron microscopic images in Figure 5A, the nanoreactors can be degraded under an acid environment. Simultaneously, the degradation time of the nanoreactor was determined by using the ICP-MS (Figures S17 and 5B). The content of Zn^{2+} from the extracted lysosomes within the glucose solution (1.0 mM. pH = 5.0) is gradually reduced, and the nanoreactors can be basically degraded in an acid environment within ~3 days.

Figures 5C and 5D show that the SERS signal of the nanoreactor gradually weakens as the acidity of the medium increases, indicating gradual degradation of the ZIF-8 skeleton structure of the nanoreactors under acidic condition, causing GOx's leakage eventually. The released GOx catalyzes the hydrolysis of glucose to generate H_2O_2, which can further etch AgNPs gradually, resulting in the weakening of the SERS signal of MBN located on AgNPs. Figure 5D shows the time evolution with the GOx releasing, derived

from the time-dependent SERS intensities (at 2,226 cm^{-1}) of the nanoreactors, indicating that GOx release is pH dependent and that this process can be completed in 2.5 h at pH 4.5. No GOx release is observed at pH = 7.0 (Figures 5D and S18). All these results prove that our nanoreactor is degradable under a mild acid condition.

The biodegradation of the nanoreactors was further evaluated in HeLa cells and tumor-bearing nude mice by using bio-TEM and *in vivo* SERS spectra. Figures 5E, 5F and S19 show the distributions of the nanoreactors within the tumor tissue of a mouse 6 h postinjection and 14 days after treatment, respectively. It can be observed that the nanoreactors, previously located in lysosomes of the tumor tissue, have been completely degraded 14 days after treatment. Figure 5G shows the photograph of a Raman laser beam (785 nm) focusing on the tumor site of a mouse at 24 h postinjection, to acquire its Raman spectra *in vivo*. As shown in Figure 5H, the tumor area of a mouse treated with the nanoreactors for 24 h exhibits strong SERS signals. However, almost no SERS signal was observed for the cancer tissue 14 days after treatment. This proves that the nanoreactors in the mice can be degraded after the therapy, which solves the common problem of the long-term accumulation *in vivo* for most nanocarriers or nanodrugs.

Conclusion

In summary, we developed an intelligent degradable nanocomposite (ZIF-8@GOx-AgNPs@MBN) composed of the GOx-enveloped ZIF-8 nanoparticles and the MBN-modified AgNPs. The nanoreactor possesses the catalysis-enhanced synergistic starvation/metal ion poisoning cancer therapy triggered *in situ* by the tumor microenvironment of lysosomes. Differentiated therapy toward tumor cells from normal cells was achieved by this strategy. This ZIF-8 nanocarrier has a high loading of GOx to ~55 wt %, and this encapsulation structure well protects GOx from the enzyme-mediated degradation *in vivo*. Meanwhile, the AgNPs@MBN component on the nanoreactor can sense glucose and GOx activity during the therapeutic process *via* SERS feedback. The signal readout in the Raman silent range is beneficial to probe pharmacodynamics and tumor microenvironment changes in a living body. In addition, this nanoreactor keeps long-persistent activity under the 4 °C storage for at least one month (Figure S20). More interestingly, this nanoreactor can be cleared effectively from the mouse body due to its excellent biodegradability, which avoids long-term toxicity and endows it with many *in vivo* applicable potentials. This work highlights a unique multi-functional nanocomposite, the MOF-supported GOx, for combating solid tumors. It also provides an extensible route to design smart catalytic cascade nanosystems for anticancer and extensive applications in biomedical fields.

Limitations of the Study

Some limitations to the findings of this study must be acknowledged. First, the limitation of this work is that the sample size of the mice studied is not large enough, so that the results obtained cannot fully accurately reflect the therapeutic effect of the nanoreactor. Second, in this study we worked with nude mice. Although its physiological characteristics are similar to those of humans, there are certain differences. Therefore, there are still some challenges in using this method for real clinical diagnosis and cancer therapy.

Electronic Supplementary Information (ESI) available: Experimental Section, characterizations of the ZIF-8@GOx-AgNPs@MBN, catalytic performance of GOx, characterization of ZIF-8@RhB, treatment effect of the nanoreactor for HeLa cells, cell viabilities of H8 cells under different treatments, comparison of H8 cells viability under 2D and 3D cell culture, evaluation of H_2O_2 content in HeLa cells, establishment of cervical tumor xenograft, H&E staining of main organs, biodistributions of Zn^{2+} and Ag^{+} in main organs, blood chemistry analyses of the tested mice, biodistributions of Zn^{2+} and Ag^{+} in extracted lysosomes, GOx release self-sensing, long-term stability of the nanoreactor.

Resource Availability

Lead Contact

Further information and requests for resources and reagents should be directed to and will be fulfilled by the Lead Contact, Shuping Xu (xusp@jlu.edu.cn).

Materials Availability

This study did not generate new unique reagents.

Data and Code Availability

This study did not generate datasets/code.

METHODS

All methods can be found in the accompanying Transparent Methods supplemental file.

SUPPLEMENTAL INFORMATION

Supplemental Information can be found online at https://doi.org/10.1016/j.isci.2020.101274.

ACKNOWLEDGMENTS

This work was supported by National Natural Science Foundation of China (grant Nos. 21873039, 21675146, 21573087,and 21573092).

AUTHOR CONTRIBUTIONS

D.S. conducted the experiments, generated figures, performed analysis and wrote the manuscript. G.Q. designed and conducted the experiments and collected and analyzed the data. K.M. performed animal experiments and collected the data. X.Q. performed animal experiments. W.X. participated in the discussion and contributed to manuscript preparation. S.X. conceptualized the project and contributed to manuscript preparation. Y.J. conceived the project, participated in the discussion, and contributed to manuscript preparation. All authors read and approved the final manuscript.

DECLARATION OF INTERESTS

The authors declare no competing interests.

Received: March 24, 2020
Revised: April 26, 2020
Accepted: June 11, 2020
Published: July 24, 2020

REFERENCES

Cai, W., Wang, J.Q., Chu, C.C., Chen, W., Wu, C.S., and Liu, G. (2019). Metal-organic framework-based stimuli-responsive systems for drug delivery. Adv. Sci. *6*, 1801526.

Chang, K., Liu, Z., Fang, X., Chen, H., Men, X., Yuan, Y., Sun, K., Zhang, X., Yuan, Z., and Wu, C. (2017). Enhanced phototherapy by nanoparticle-enzyme via generation and photolysis of hydrogen peroxide. Nano Lett. *17*, 4323–4329.

Cheng, H., Jiang, X.Y., Zheng, R.R., Zuo, S.J., Zhao, L.P., Fan, G.L., Xie, B.R., Yu, X.Y., Li, S.Y., and Zhang, X.Z. (2019). A biomimetic cascade nanoreactor for tumor targeted starvation therapy amplified Chemotherapy. Biomaterials *195*, 75–85.

Cheng, L., Liu, J.J., Gu, X., Gong, H., Shi, X.Z., Liu, T., Wang, C., Wang, X.Y., Liu, G., Xing, H.Y., et al. (2014). PEGylated WS2 nanosheets as a multifunctional theranostic agent for in vivo dual-modal CT/photoacoustic imaging guided photothermal therapy. Adv. Mater. *26*, 1886–1893.

Chen, G.S., Huang, S.M., Kou, X.X., Wei, S.B., Huang, S.Y., Jiang, S.Q., Shen, J., Zhu, F., and Ouyang, G.F. (2019). A convenient and versatile amino-acid-boosted biomimetic strategy for the nondestructive encapsulation of biomacromolecules within metal–organic frameworks. Angew. Chem. Int. Ed. *58*, 1463–1467.

Chen, L.M., Li, H.J., He, H.L., Wu, H.X., and Jin, Y.D. (2015). Smart plasmonic glucose nanosensors as generic theranostic agents for targeting-free cancer cell screening and killing. Anal. Chem. *87*, 6868–6874.

Chen, T.T., Yi, J.T., Zhao, Y.Y., and Chu, X. (2018). Biomineralized metal–organic framework nanoparticles enable intracellular delivery and endo-lysosomal release of native active proteins. J. Am. Chem. Soc. *140*, 9912–9920.

Feng, Y.F., Wang, H.R., Zhang, S.N., Zhao, Y., Gao, J., Zheng, Y.Y., Zhao, P., Zhang, Z.J., Zaworotko, M.J., Cheng, P., et al. (2018). Antibodies@MOFs: an in vitro protective coating for preparation and storage of biopharmaceuticals. Adv. Mater. *140*, 1805148.

Fu, L.H., Qi, C., Lin, J., and Huang, P. (2018). Catalytic chemistry of glucose oxidase in cancer diagnosis and treatment. Chem. Soc. Rev. *47*, 6454–6472.

Gao, H., Zhao, L., Wang, H., Xie, E.J., Wang, X.H., Wu, Q., Yu, Y.Y., He, X.Y., Ji, H.B., Rink, L., et al. (2017). Metal transporter Slc39a10 regulates susceptibility to inflammatory stimuli by controlling macrophage survival. Proc. Natl. Acad. Sci. U S A *114*, 12940–12945.

Gao, L.H., Chen, Q., Gong, T.T., Liu, J.H., and Li, C.X. (2019). Recent advancement of imidazolate framework (ZIF-8) based nanoformulations for synergistic tumor therapy. Nanoscale *11*, 21030–21045.

Gazaryan, I.G., Krasinskaya, I.P., Kristal, B.S., and Brown, A.M. (2007). Zinc irreversibly damages major enzymes of energy production and antioxidant defense prior to mitochondrial permeability transition. J. Biol. Chem. *282*, 24373–24380.

Ge, J., Lan, M., Zhou, B., Liu, W., Guo, L., Wang, H., Jia, Q., Niu, G., Huang, X., Zhou, H., et al. (2014). A graphene quantum dot photodynamic therapy agent with high singlet oxygen generation. Nat. Commun. *5*, 4596–4603.

Han, X., Huang, J., Jing, X., Yang, D., Lin, H., Wang, Z., Li, P., and Chen, Y. (2018). Oxygen-deficient black titania for synergistic/enhanced sonodynamic and photoinduced cancer therapy at near infrared-II biowindow. ACS Nano *12*, 4545–4555.

Hsu, P.P., and Sabatini, D.M. (2008). Cancer cell metabolism: warburg and beyond. Cell *134*, 703–707.

Huo, M.F., Wang, L.Y., Chen, Y., and Shi, J.L. (2017). Tumor-selective catalytic nanomedicine

by nanocatalyst delivery. Nat. Commun. *8*, 357–369.

Kotagiri, N., Sudlow, G.P., Akers, W.J., and Achilefu, S. (2015). Breaking the depth dependency of phototherapy with Cerenkov radiation and low-radiance-responsive nanophotosensitizers. Nat. Nanotechnol. *10*, 370–379.

Liang, S., Deng, X.R., Chang, Y., Sun, C.Q., Shao, S., Xie, Z.X., Xiao, X., Ma, P., Zhang, H.Y., Cheng, Z.Y., et al. (2019). Intelligent hollow Pt-CuS Janus architecture for synergistic catalysis-enhanced sonodynamic and photothermal cancer therapy. Nano Lett. *19*, 4134–4145.

Lin, H., Chen, Y., and Shi, J. (2018). Nanoparticle-triggered in situ catalytic chemical reactions for tumour-specific therapy. Chem. Soc. Rev. *47*, 1938–1958.

Link, T.A., and Jagow, G. (1995). Zinc ions inhibit the QP center of bovine heart mitochondrial bc1 complex by blocking a protonatable group. J. Biol. Chem. *270*, 25001–25006.

Lin, L.S., Huang, T., Song, J.B., Ou, X.Y., Wang, Z.T., Deng, H.Z., Tian, R., Liu, Y.J., Wang, J.F., Liu, Y., et al. (2019). Synthesis of copper peroxide nanodots for H_2O_2 self-supplying chemodynamic therapy. J. Am. Chem. Soc. *141*, 9937–9945.

Li, Y., Wen, T., Zhao, R., Liu, X., Ji, T., Wang, H., Shi, X., Shi, J., Wei, J., Zhao, Y., et al. (2014). Localized electric field of plasmonic nanoplatform enhanced photodynamic tumor therapy. ACS Nano *8*, 11529–11542.

Manev, H., Kharlamov, E., Uz, T., Mason, R.P., and Cagnoli, C.M. (1997). Characterization of zinc-induced neuronal death in primary cultures of rat cerebellar granule cells. Exp. Neurol. *146*, 171–178.

Ma, Y.C., Zhao, Y.Y., Bejjanki, N.K., Tang, X.F., Jiang, W., Dou, J.X., Khan, M.I., Wang, Q., Xia, J.X., Liu, H., et al. (2019). Nanoclustered cascaded enzymes for targeted tumor starvation and deoxygenation-activated chemotherapy without systemic toxicity. ACS Nano *13*, 8890–8902.

Qi, G.H., Zhang, Y., Xu, S.P., Li, C.P., Wang, D.D., Li, H.J., and Jin, Y.D. (2018). Nucleus and mitochondria targeting theranostic plasmonic surface-enhanced Raman spectroscopy nanoprobes as a means for revealing molecular stress response differences in hyperthermia cell death between cancerous and normal Cells. Anal. Chem. *90*, 13356–13364.

Qi, G.H., Li, H.J., Zhang, Y., Li, C.P., Xu, S.P., Wang, M.M., and Jin, Y.D. (2019). Smart plasmonic nanorobot for real-time monitoring cytochrome c release and cell acidification in apoptosis during electrostimulation. Anal. Chem. *91*, 1408–1415.

Schoedel, A., Li, M., Li, D., O'Keeffe, M., and Yaghi, O.M. (2016). Structures of metal–organic frameworks with rod secondary building Units. Chem. Rev. *116*, 12466–12535.

Shen, Y.T., Liang, L.J., Zhang, S.Q., Huang, D.S., Zhang, J., Xu, S.P., Liang, C.Y., and Xu, W.Q. (2018). Organelle-targeting surface-enhanced Raman scattering (SERS) nanosensors for subcellular pH sensing. Nanoscale *10*, 1622–1630.

Skulachev, V.P., Chistyakov, V.V., Jasaitis, A.A., and Smirnova, E.G. (1967). Inhibition of the respiratory chain by zinc ions. Biochem. Biophys. Res. Commun. *26*, 1–6.

Soenen, S.J., Parak, W.J., Rejman, J., and Manshian, B. (2015). (Intra)Cellular stability of inorganic nanoparticles: effects on cytotoxicity, particle functionality, and biomedical applications. Chem. Rev. *115*, 2109–2135.

Song, G.S., Chen, Y.Y., Liang, C., Yi, X., Liu, J.J., Sun, X.Q., Shen, S.D., Yang, K., and Liu, Z. (2016). Catalase-loaded TaOx nanoshells as bio-nanoreactors combining high-Z element and enzyme delivery for enhancing radiotherapy. Adv. Mater. *28*, 7143–7148.

Tang, Z.M., Liu, Y.Y., He, M.Y., and Bu, W.B. (2019). Chemodynamic therapy: tumour microenvironment-mediated fenton and fenton-like reactions. Angew. Chem. Int. Ed. *58*, 946–956.

Wang, C., Ye, Y., Hochu, G.M., Sadeghifar, H., and Gu, Z. (2016). Enhanced cancer immunotherapy by microneedle patch-assisted delivery of anti-PD1 antibody. Nano Lett. *16*, 2334–2340.

Wang, M.M., Tang, Y.F., and Jin, Y.D. (2019a). Modulating catalytic performance of metal–organic framework composites by localized surface plasmon resonance. ACS Catal. *9*, 11502–11514.

Wang, M., Wang, D.M., Chen, Q., Li, C.X., Li, Z.Q., and Lin, J. (2019b). Recent advances in glucose-oxidase-based nanocomposites for tumor therapy. Small *15*, e1903895.

Wang, W.G., Cheng, Y.H., Yu, P., Wang, H.R., Zhang, Y., Xu, H.H., Ye, Q.S., Yuan, A.H., Hu, Y.Q., and Wu, J.H. (2019c). Perfluorocarbon regulates the intratumoural environment to enhance hypoxia-based agent efficacy. Nat. Commun. *10*, 1580–1590.

Yang, B., Chen, Y., and Shi, J. (2019). Reactive oxygen species (ROS)-based nanomedicine. Chem. Rev. *119*, 4881–4985.

Ying, H.Q., Kimmelman, A.C., Lyssiotis, C.A., Hua, S.J., Chu, G.C., Sananikone, E., Locasale, J.W., Son, J.Y., Zhang, H.L., Coloff, J.L., et al. (2012). Oncogenic Kras maintains pancreatic tumors through regulation of anabolic glucose metabolism. Cell *149*, 656–670.

Zhang, C., Zhao, K., Bu, W.B., Ni, D.L., Liu, Y.Y., Feng, J.W., and Shi, J.L. (2015). Marriage of scintillator and semiconductor for synchronous radiotherapy and deep photodynamic therapy with diminished oxygen dependence. Angew. Chem. Int. Ed. *54*, 1770–1774.

Zhang, L., Wang, Z.Z., Zhang, Y., Cao, F.F., Dong, K., Ren, J.S., and Qu, X.G. (2018a). Erythrocyte membrane cloaked metal–organic framework nanoparticle as biomimetic nanoreactor for starvation-activated colon cancer therapy. ACS Nano *12*, 10201–10211.

Zhang, L., Wan, S.S., Li, C.X., Xu, L., Cheng, H., and Zhang, X.Z. (2018b). An adenosine triphosphate-responsive autocatalytic fenton nanoparticle for tumor ablation with self-supplied H_2O_2 and acceleration of Fe(III)/Fe(II) conversion. Nano Lett. *18*, 7609–7618.

iScience, Volume *23*

Supplemental Information

Tumor Microenvironment-Activated Degradable Multifunctional Nanoreactor for Synergistic Cancer Therapy and Glucose SERS Feedback

Dan Sun, Guohua Qi, Kongshuo Ma, Xiaozhang Qu, Weiqing Xu, Shuping Xu, and Yongdong Jin

Supporting information

Tumor Microenvironment Activated Degradable Multifunctional Nanoreactor for Synergistic Cancer Therapy and Glucose SERS Feedback

Dan Sun,[1,#] Guohua Qi,[2,#] Kongshuo Ma,[2,3] Xiaozhang Qu,[1] Weiqing Xu,[1] Shuping Xu,[1,*] Yongdong Jin[2,3,*]

[1] State Key Laboratory of Supramolecular Structure and Materials, Institute of Theoretical Chemistry, College of Chemistry, Jilin University, Changchun 130012, P. R. China.
[2] State Key Laboratory of Electroanalytical Chemistry, Changchun Institute of Applied Chemistry, Chinese Academy of Sciences, Changchun 130022, Jilin, P. R. China.
[3] University of Science and Technology of China, Hefei 230026, P. R. China.

[#] Dan Sun and Guohua Qi contributed equally to this article.
* Correspondence: xusp@jlu.edu.cn (X. S.), ydjin@ciac.ac.cn (J. Y.)

1. Characterizations of the ZIF-8@GOx-AgNPs@MBN

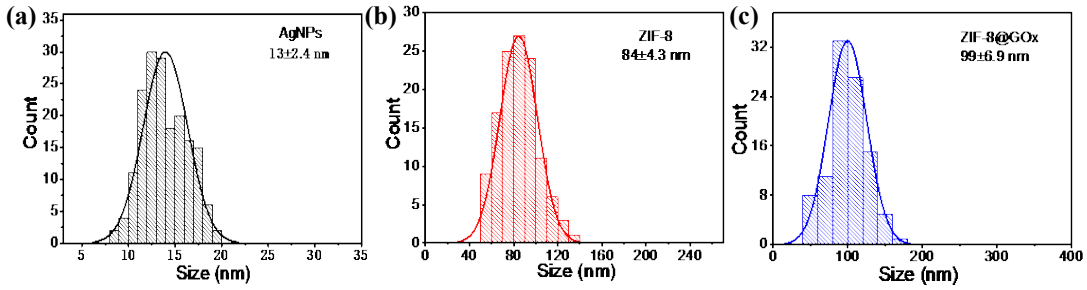

Supplemental Figure 1: Related to Figure 1

Figure S1. The statistic particle sizes of (a) AgNPs, (b) ZIF-8 and (c) ZIF-8@GOx, respectively, used in this study.

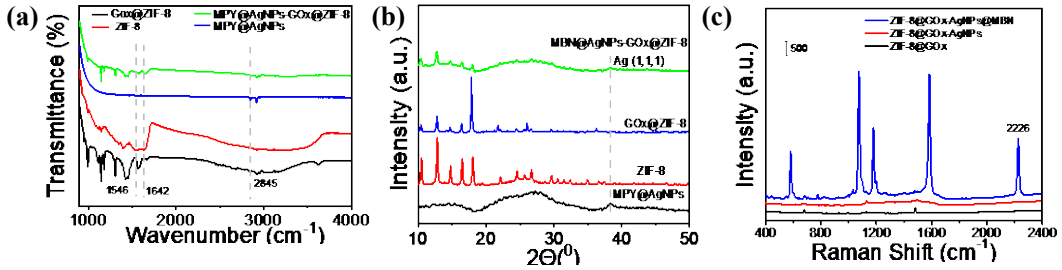

Supplemental Figure 2: Related to Figure 1

Figure S2. (a) FT-IR spectra and (b) XRD patterns of the AgNPs@MBN, ZIF-8, ZIF-8@GOx, and the ZIF-8@GOx-AgNPs@MBN nanoreactors, respectively. (c) SERS spectra of ZIF-8@GOx, ZIF-8@GOx-AgNPs, and the nanoreactors, respectively. A laser wavelength of 632.8 nm and an acquisition time of 5 s were used for the SERS measurements.

Figure S2 shows the FTIR analysis of the AgNPs@MBN, ZIF-8, ZIF-8@GOx, and the ZIF-8@GOx-AgNPs@MBN. By comparison FT-IR spectrum of the nanoreactors with others (Figure S2), we can find that the bands from ~2840 to 2850 cm^{-1} and from ~1630 to 1650 cm^{-1}, ascribed to the amide I and II bands respectively, are identified, indicating the successful fixing of the AgNPs@MBN on the surface of ZIF-8@GOx.

Moreover, the XRD data confirm that the ZIF-8@GOx maintained the same crystalline form as the pure ZIF-8 NPs (Figure S2b), suggesting that the hybridization preparation did not alter the crystalline structure of ZIF-8. Moreover, the peaks of ZIF-8@GOx-AgNPs@MBN centered at 8.3°, 18.4° and 28.3°, 30.4° indicate the

co-existence of the standard Bragg reflections of ZIF-8 and metallic AgNPs (e.g., 111, 200), testifying again the complex structure of the ZIF-8@GOx-AgNPs@MBN.

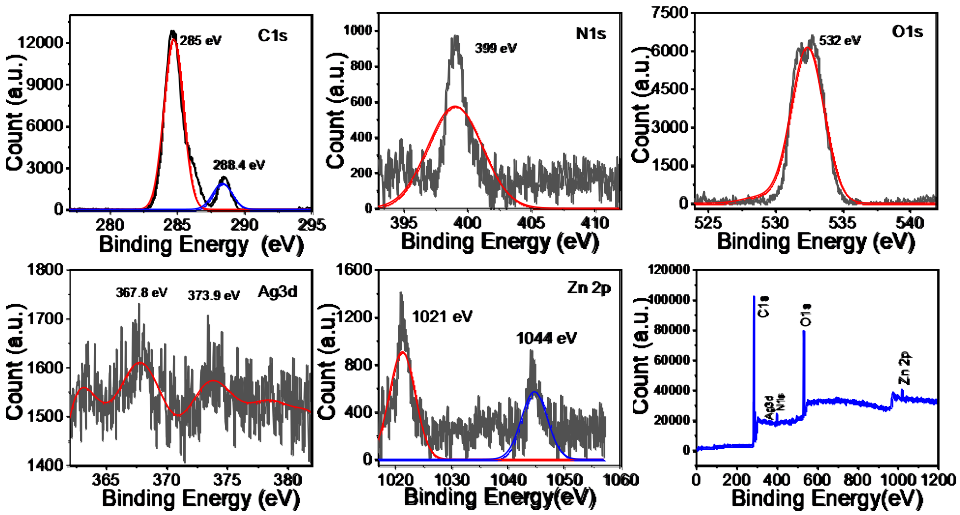

Supplemental Figure 3: Related to Figure 1

Figure S3. The XPS spectra of C 1s, N 1s, O 1s, Ag 3d, and Zn 2p of the nanoreactor, respectively. The XPS spectra were carried out to analyze the valence state of the elements of the ZIF-8@GOx-AgNPs@MBN nanoreactor. The peaks located at 285 eV and 288.4 eV are attributed to C 1s and the peaks at 399 and 532 eV belong to N 1s and O 1s, respectively. The peak located at 1044 eV is Zn 2p of the ZIF-8 (Figure S3).

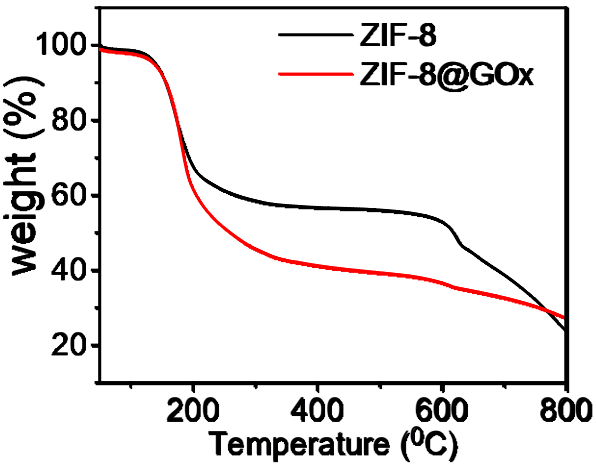

Supplemental Figure 4: Related to Figure 1

Figure S4. Thermogravimetric analysis (TGA) of ZIF-8 and ZIF-8@GOx.

2. Catalytic performance of GOx

$$\text{Glucose} + O_2 + H_2O \xrightarrow{GOx} \text{Gluconic acid} + H_2O_2 \quad (1)$$

$$H_2O_2 + \text{TMB (colorless)} \xrightarrow{HRP} \text{ox-TMB (colored)} + H_2O \quad (2)$$

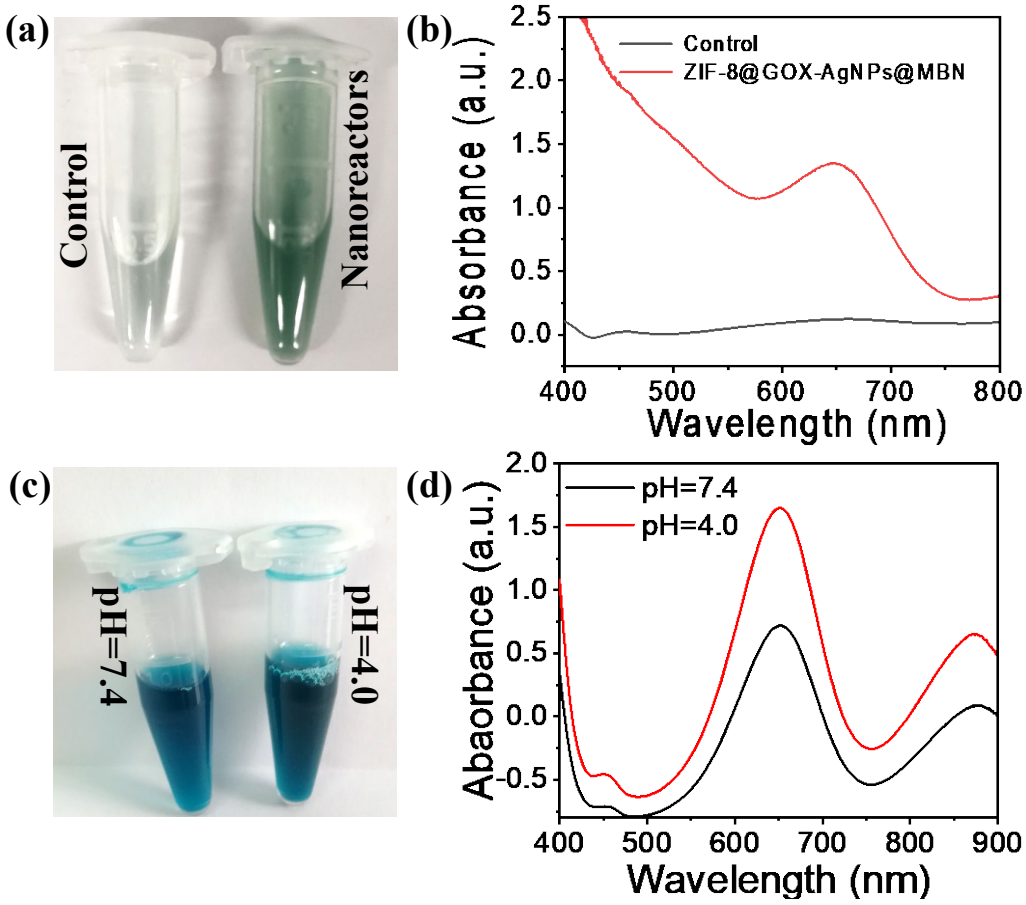

Supplemental Figure 5: Related to Figure 2

Figure S5. The photograph under control vs nanoreactor (a) and the pH=4.0, 7.4, respectively (c).UV−vis absorption spectra of the oxidized TMB (oxTMB) produced under control vs nanoreactor (b) and the pH=4.0, 7.4, respectively (d).

In order to find the pH value with the best catalytic activity of GOx, we firstly conducted a chromogenic reaction of tetramethyl benzidine (TMB) under different enzyme activities of GOx and obtained a good linear response to GOx activity in a range from 10 to 1000 U/mL (Figure S6b) with regression equation of y=0.766x+0.12. Then, the UV−vis absorption spectra of the oxidized TMB (oxTMB) produced under different pH were carried out. According to the Figure S6c&d, the optimum pH for GOx activity is ～4 in vitro and the activity of GOx is about 616.6 U/mL in the acidic environment of the tumor.

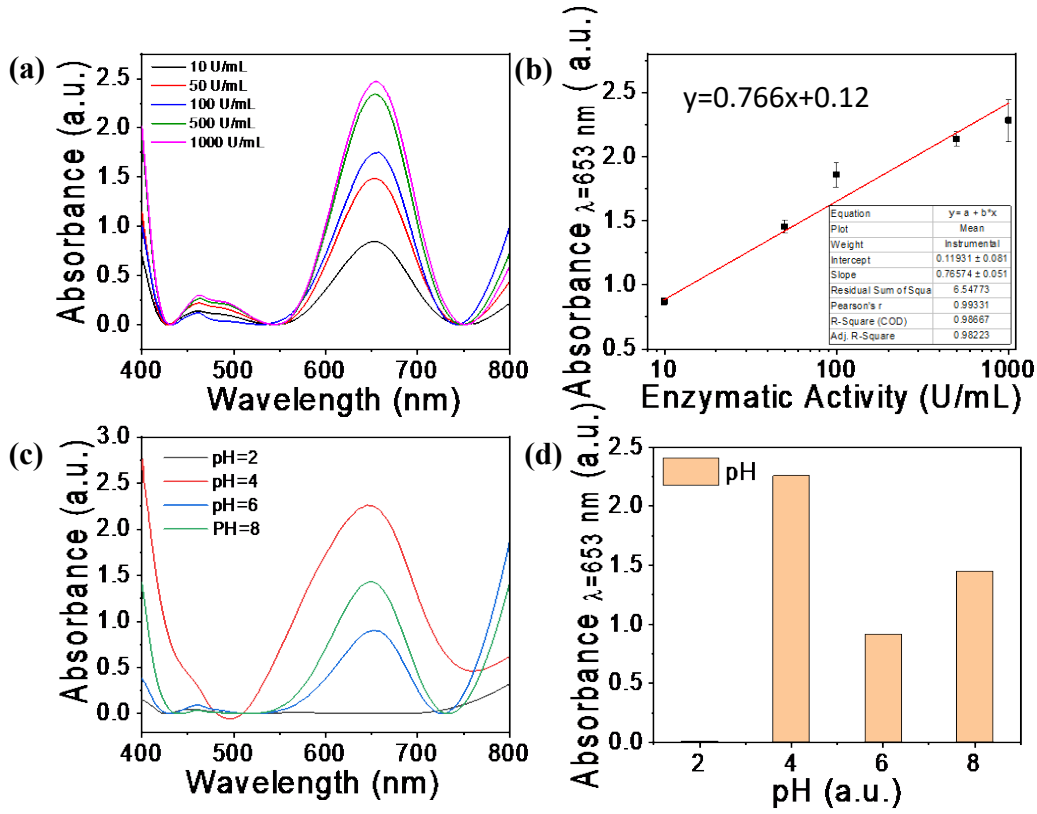

Supplemental Figure 6: Related to Figure 2

Figure S6. (a) UV−vis absorption spectra of the oxidized TMB (oxTMB) produced under different enzyme activities of GOx. (b) The plot of the absorbance intensity at 653 nm with the enzyme activities of GOx. (c) UV−vis absorption spectra of the oxidized TMB (oxTMB) produced under different pH and (d) corresponding histogram of absorbance intensity at 653 nm vs pH.

To prove whether the activity of GOx is affected by 5% SDS (w/w) aqueous solution at 50℃, we determined the UV−vis absorption spectra of the oxidized TMB (oxTMB) produced under different temperature. As shown in Figure S7a&b of revised supporting information, GOx maintained 85.8% activity at 50℃ compared to room temperature.

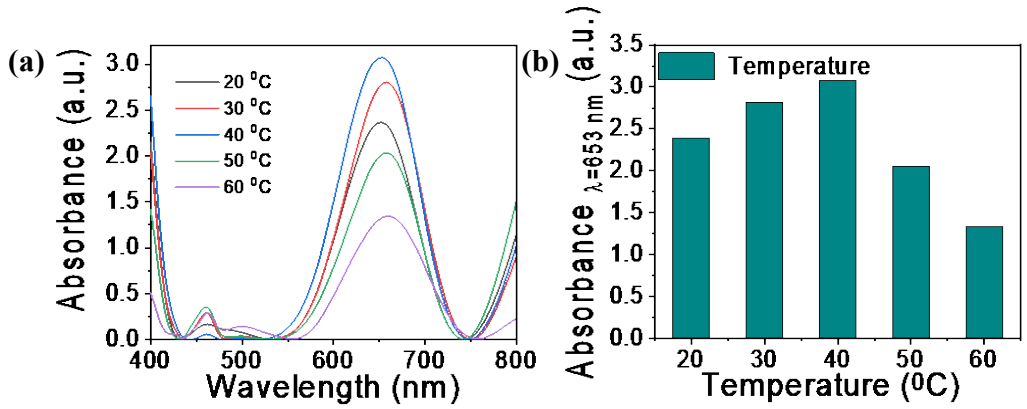

Supplemental Figure 7: Related to Figure 2

Figure S7. (a) UV−vis absorption spectra of the oxidized TMB (oxTMB) produced under different temperature and (b) corresponding histogram of absorbance intensity at 653 nm vs temperature.

3. Characterizations of ZIF-8@RhB

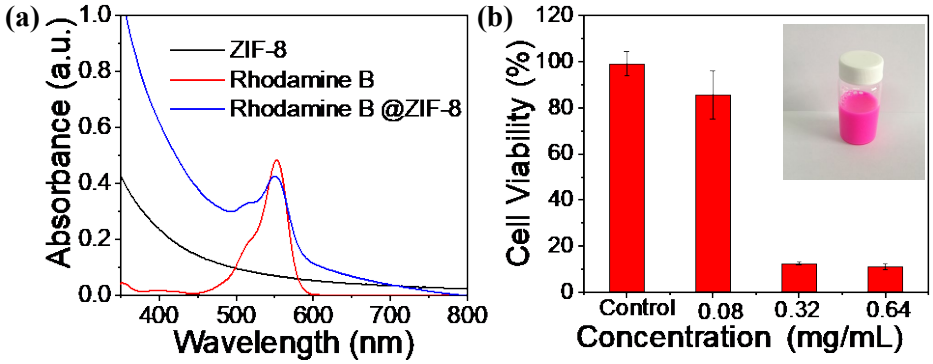

Supplemental Figure 8: Related to Figure 2

Figure S8. (a) UV−vis absorption spectra of ZIF-8, Rhodamine B (RhB) and RhB@ZIF-8, respectively. The absorption band at 552 nm is originated from RhB. (b) Cell viabilities of different concentrations RhB@ZIF-8 pretreated HeLa cells for 24 h, determined by the standard MTT assay, showing that an optimized concentration is 0.08 mg/mL. The inset shows a photograph of RhB@ZIF-8.

4. Treatment effect of the nanoreactor for HeLa cells

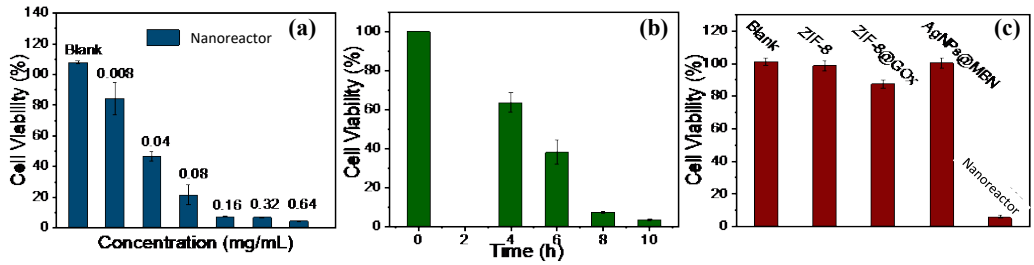

Supplemental Figure 9: Related to Figure 3

Figure S9. (a) HeLa cells viabilities incubated with different concentrations of the ZIF-8@GOx-AgNPs@MBN nanoreactors. (b) Cell viabilities of the nanoreactor (0.8 mg/mL)-pretreated HeLa cells for different incubation time. (c) The viability of the HeLa cells treated with different nanoparticles, including blank, ZIF-8, ZIF-8@GOx, AgNPs@MBN and the ZIF-8@GOx-AgNPs@MBN nanoreactors.

5. Cell viabilities of H8 cells under different treatments

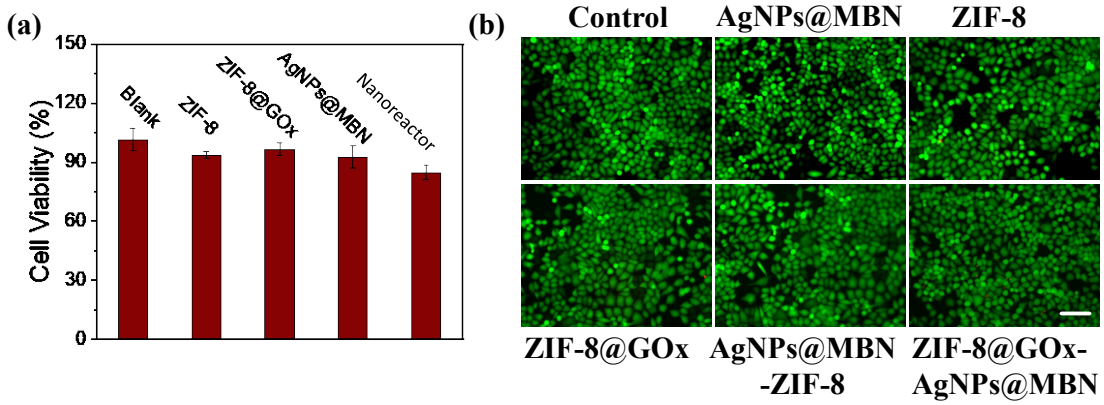

Supplemental Figure 10: Related to Figure 3

Figure S10. (a) The cell viability of H8 cells after the treatment with different nanomaterials, including control, ZIF-8, ZIF-8@GOx, AgNPs@MBN and ZIF-8@GOx-AgNPs@MBN. (b) The corresponding fluorescent images of H8 cells underwent different treatments (cells were stained by Calcein-AM/PI; green, alive; red, dead). All of the scale bars are 60 μm.

6. Comparison of H8 cells viability under 2D and 3D cell culture

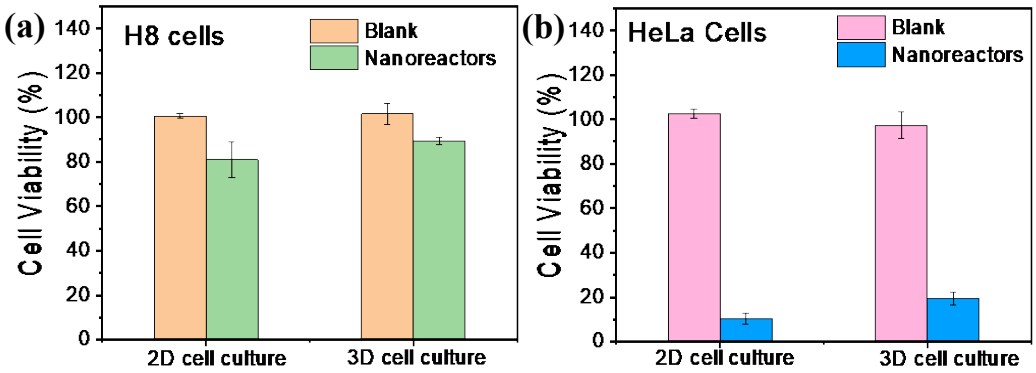

Supplemental Figure 11: Related to Figure 3

Figure S11. The viability of H8 cells (a), HeLa (b) under 2D and 3D cell culture. The concentration of the nanoreactor used is 0.8 mg/mL, and incubation time is 8 h.

7. Evaluation of H_2O_2 content in HeLa cells

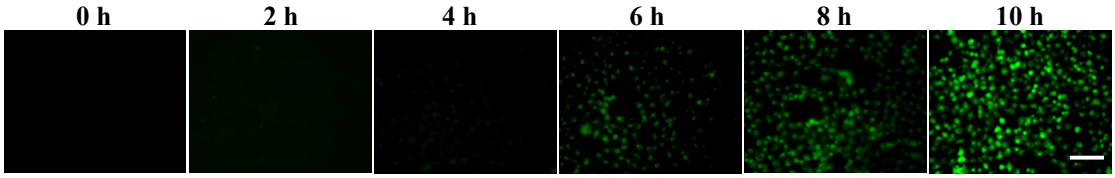

Supplemental Figure 12: Related to Figure 3

Figure S12. The confocal fluorescent images of HeLa cells after co-incubation with the ZIF-8@GOx-AgNPs@MBN nanoreactors for different periods. All of the scale bars are 50 μm. Cells were stained with RDPP $[Ru(dpp)_3]Cl_2$.

8. Establishment of cervial tumor xenograft

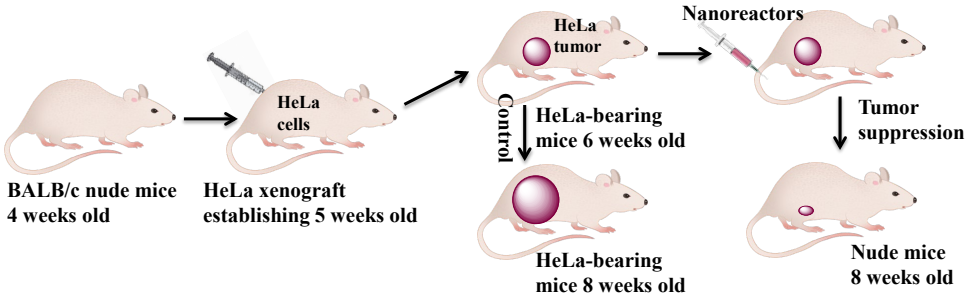

Supplemental Figure 13: Related to Figure 4

Figure S13. Schematic illustration of the cervial tumor xenograft establishment, blank and synergistic chemo-starving cancer therapy procedures, and therapeutic outcome.

9. H&E staining of main organs

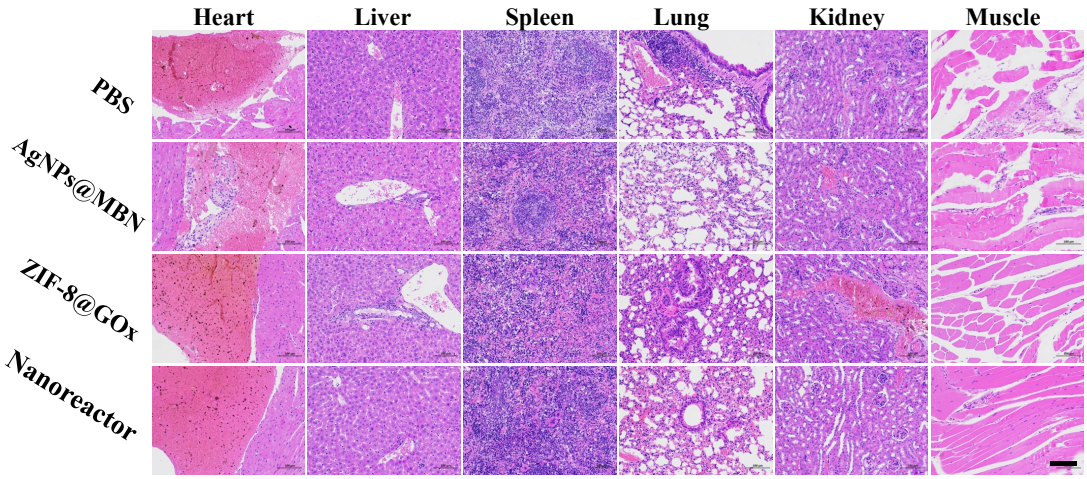

Supplemental Figure 14: Related to Figure 5

Figure S14. H&E staining images of the main organs after the different treatments. All of the scale bars are 100 μm.

10.Biodistributions of Zn^{2+} and Ag^{+} in main organs

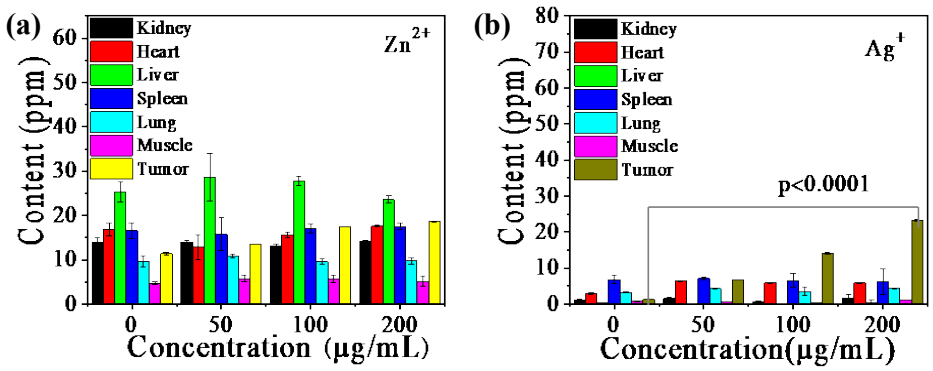

Supplemental Figure 15: Related to Figure 5

Figure S15. Biodistributions of Zn^{2+} (a) and Ag^{+} (b) in main organs and tumors on the 14th day of intravenous administrations of the nanoreactors with different dosages.

11. Blood chemistry analyses of the tested mice

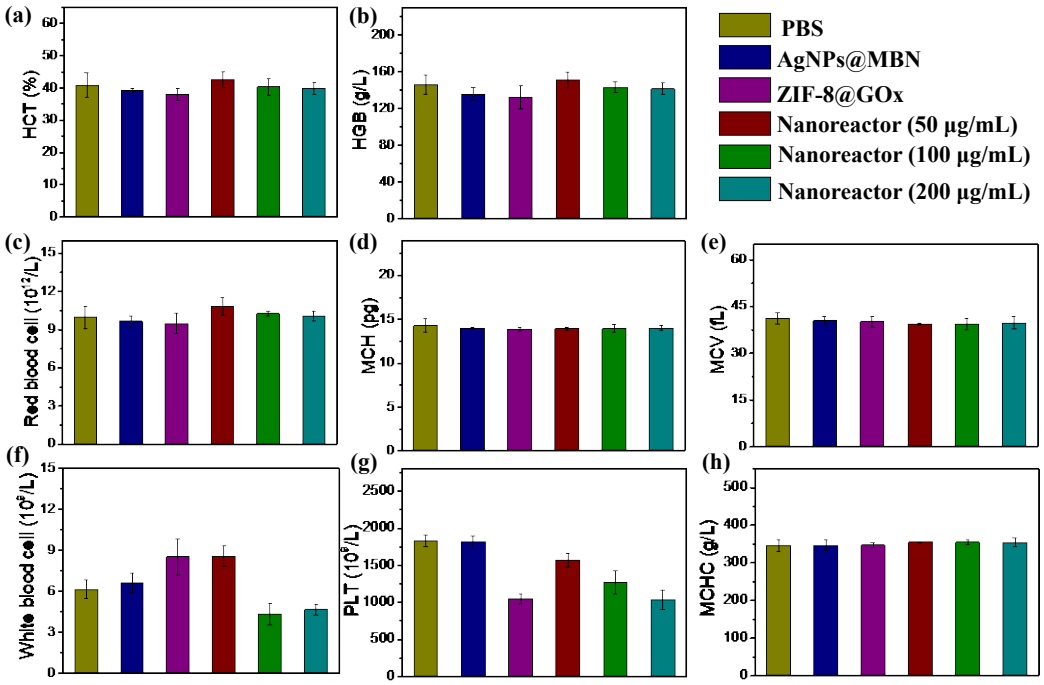

Supplemental Figure 16: Related to Figure 5

Figure S16. (a) HCT, (b) Hemoglobin, (c) RBC, (d) MCH, (e) HCV, (f) WBC, (g) PLT and (h) MCHC levels of the tested mice in all groups. Mean values and error bars are from three trials.

Supplemental Table 1: Related to Figure 5

Table S1: The trace element levels of mice in all groups. Each sample is measured three times.

	Pb (μg/L)	Zn (μmol/L)	Cu (μmol/L)	Fe (mmol/L)	Ca (mmol/L)	Mg (mmol/L)
PBS	44	56.58	22.90	7.12	1.74	1.58
AgNPs@MBN	42	58.79	13.60	7.24	1.68	1.58
ZIF-8@GOx	38	60.7	13.42	7.83	1.44	1.46
Nanoreactor (50 μg/mL)	28	58.12	23.93	7.34	1.65	1.61
Nanoreactor (100 μg/mL)	29	66.88	21.85	7.84	1.77	1.65
Nanoreactor (200 μg/mL)	29	56.68	20.59	7.13	1.60	1.52

12.Biodistributions of Zn^{2+} and Ag^{+} in extracted lysosomes

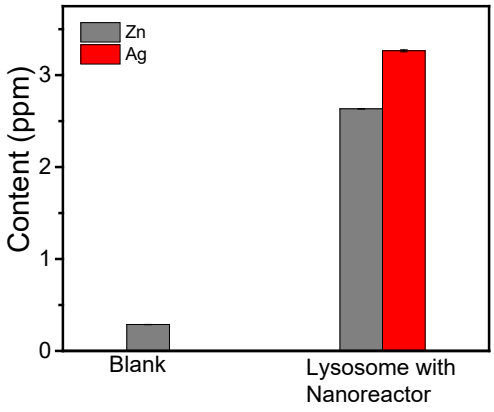

Supplemental Figure 17: Related to Figure 5

Figure S17. Comparison of the biodistributions of Zn^{2+} and Ag^{+} in blank and extracted lysosomes with the nanoreactors.

13.GOx release self-sensing

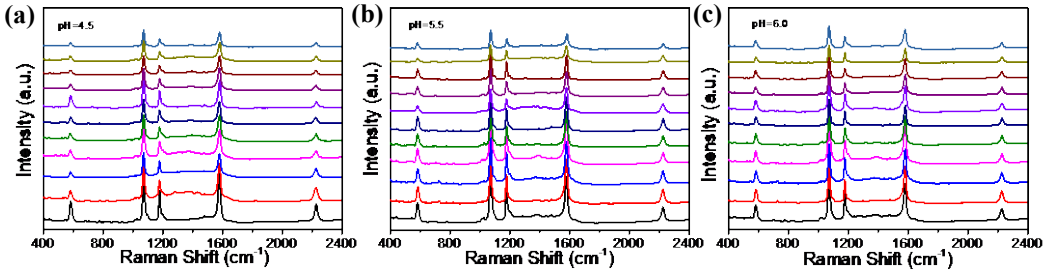

Supplemental Figure 18: Related to Figure 5

Figure S18. SERS spectra of MBN on the nanoreactors after they reacted with 5.0 mM of glucose at different pHs of 4.5 (a), 5.5 (b), and 6.0 (c) with different reaction time (0-5 h), recorded every 0.5 h.

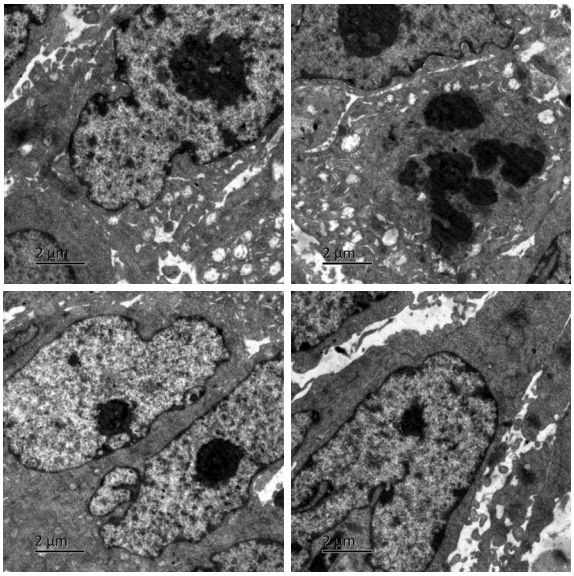

Supplemental Figure 19: Related to Figure 5

Figure S19. Bio-TEM images of the tumor tissues after 14 d postinjection of the nanoreactor.

14.Long-term stability of the nanoreactor

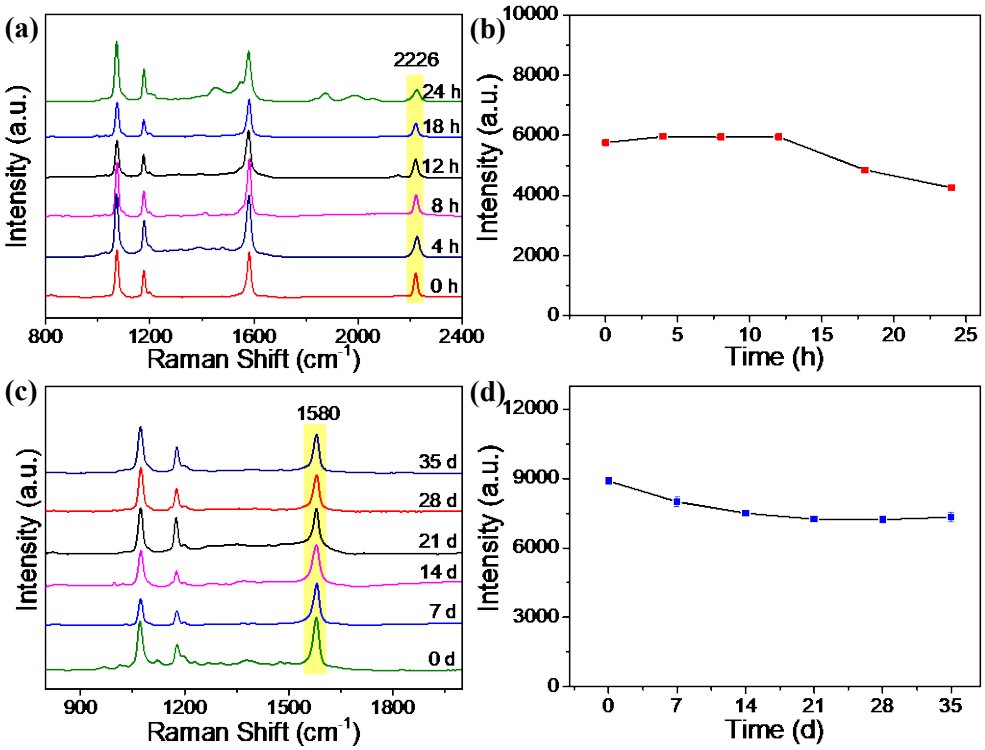

Supplemental Figure 20: Related to Figure 5

Figure S20. (a) SERS spectra of MBN on the nanoreactor kept in 50% serum at 37 °C for different time (0, 4, 8, 12, 18 and 24 h). (b) SERS intensity variation at 2226 cm^{-1} with different incubation time. SERS spectra (c) and intensity at 1580 cm^{-1} (d) of the nanoreactor along with the

storage time (at 4 ºC), recorded every one week.

This nanoreactor keeps long-persistent activity under the 4 ºC storage for at least one month (Figure S20).

Transparent Methods

Materials and Instrument

4-mercaptobenzonitrile (MBN) was purchased from Nanjing Shengsai Chemical Co., Ltd. 3-(4, 5-Dimethylthiazol-2-yl)-2, 5-diphenyltetrazolium bromide (MTT) and dimethyl sulfoxide (DMSO) were bought from Key-GenBioTech. Hexahydrate and zinc nitrate ($Zn(NO_3)_2$•$6H_2O$), 2-methylimidazole, sodium chloride (NaCl), potassium chloride (KCl), Calcein-AM/ propidium iodide (PI), sodium borohydride ($NaBH_4$), sodium citrate ($C_6H_5Na_3O_7$), glucose oxidase (GOx), silver nitrate ($AgNO_3$), adenosine triphosphate (ATP), alkaline phosphatase, troponin, prostate specific antigen (PSA), cytochrome c, trypsin, glutathione (GSH) and glucose were purchased from Aladdin Industrial Corporation (Shanghai, China). Caspase-3 was purchased from the Wuhan Cloud Clone Corp. Hoechst 33342 and LysoSensor™ Green were obtained from Invitrogen (Carlsbad, CA). Rhodamine B (RhB) and sodium dodecylsulpfate ($CH_3(CH_2)_{11}OSO_3Na$) were bought from Beijing Chemical Works. 7-AAD/Annexin-V-APC was purchased from the Thermo Fisher Scientific Biological Co., Ltd. The Dulbecco's modified Eagle's medium (DMEM), antibiotic solution, fetal bovine serum (FBS) and 0.25% trypsin/2.2 mM EDTA solution were purchased from Biological Industries. The lysosomal extraction kit was purchased from Sigma-Aldrich (USA). All the solutions were prepared through the ultrapure water (DI water) which was obtained using a Millipore Milli-Q water purification system (Billerica, MA), with an electric resistance >18.25 MΩ.

The morphologies of the ZIF-8 and AgNPs were characterized by the transmission electron microscope (TEM, Hitachi 600), and their composite was imaged by the high-angle annular dark-field (HAADF)-STEM and elemental mapping. The UV-vis absorption spectra were obtained with a Lambda 750 spectrophotometer (Perkin-Elmer). The concentrations of the nanoreactors and metal elements were detected using the inductively coupled plasma mass spectrometry (ICP-MS, Thermo Scientific Icap 6300). The dynamic light scattering (DLS, Zetasizer Nano ZS 90,

British Ma Erwen Co., Ltd.) was used for the Zeta potential measurements. The chemical compositions of the samples were conducted by X-ray photoelectron spectroscopy (XPS) (Escalab 250Xi, Thermo Fisher Scientific). The X-ray Irradiator (D8 Advance) was from the Bruker. The living cell fluorescent images were performed with an inverted microscope (Leica DMI6000B, Germany). The Fourier transform infrared (FTIR) spectrum was performed using a Bruker Vertex 80 V spectrometer. SERS measurements were carried out using a Horiba Jobin Yvon Aramis spectrometer at 632.8 nm from a laser power of ~7 mW and an accumulation time of 5 s per time. Thermo gravimetric analysis (TGA) was performed using a TG 209 F1 Libra thermal gravimetric analyzer (Netzsch, Germany). Flow apoptosis assay was carried out using a BD FACSCanto II analytical flow cytometry.

Synthesis of the ZIF-8 nanoparticles (NPs)

The ZIF-8 nanocrystals were prepared using the previously reported work (Pan et al., 2011). Firstly, the two solutions were all filtered by filter paper before mixing. Typically, 1.17 g of zinc nitrate (3.95 mmol) in 8 mL DI water was added into a solution of 2-methylimidazole (22.70 g, 276.50 mmol) in 80 mL of DI water to ensure the molar ratio of 2-methylimidazole to zinc as 70:1. Then, the product was collected by repeated centrifugation (8000 rpm, 10 min) and wash by DI water for three times.

Preparation of glucose oxidase (GOx) payloaded ZIF-8 NPs

Firstly, 0.117 g of zinc nitrate was dissolved into 0.8 mL of DI water, and then 10 mg of GOx was added into the zinc nitrate solution to stir for 10 min at 30℃. After that, 2.27 g of 2-methylimidazole in 8 mL of DI water was added into the mixed solution under vigorous stirring and incubated at 30℃ for 10 min. The resulting GOx payloaded ZIF-8 NPs (ZIF-8@GOx) were centrifuged at 8000 rpm for 10 min, followed by twice wash with DI water. They were then cleaned by a 5% SDS (w/w) aqueous solution at 50℃ to remove free GOx on the surface. Finally, the ZIF-8@GOx NPs were stored in 4℃ for use.

Synthesis of AgNPs and AgNPs@MBN

The AgNPs were prepared according to the reported literature (Agnihotri et al., 2014). Typically, the fresh aqueous solution of $NaBH_4$ (1.00 mM, 1.0 mL) and sodium citrate (3.55 mM, 1.0 mL) were added into 93.0 mL of DI water to stir at 60℃ in the dark for 30 min. Next, 1.0 mL of $AgNO_3$ (1.00 mM) was added drop-wise to the mixture. Subsequently, the temperature was raised to 90℃ and then the pH of the solution was adjusted to 10.5 by NaOH (0.1 M). The solution was kept boiling for 20 min until the solution color changed to greyish green. The AgNPs were centrifuged three times at 12000 rpm for 10 min, and finally re-dispersed into DI water and stored at 4℃ for use.

MBN was chosen as the Raman reporter. 4-MBN were conjugated to AgNPs via the Ag−S bond. Briefly, 100 μL of 2mM 4-MBN were added to 2 mL AgNPs, followed by incubation for 24 h. Excess 4-MBN were then removed by centrifugation at 12000 rpm for 10 min. The resultant 4-MBN-modified AgNPs were washed and re-dispersed in deionized water.

Preparation of nanoreactor

The nanoreactors were fabricated *via* the electrostatic assembly of the ZIF-8@GOx NPs and the AgNPs@MBN since their surface charges are adverse according to the Zeta potential characterization (Fig. 1g). In a typical preparation, 1.0 mL of ZIF-8@GOx NPs (0.8 mg/mL) was mixed with 10 mL of AgNPs@MBN (2.5×10^{-5} M) and the mixture was kept stirring for 24 h. Subsequently, the nanoreactors of ZIF-8@GOx-AgNPs were three times centrifuged at 7000 rpm for 10 min to remove free AgNPs@MBN and the produced nanoreactors were then stored in 4℃ for use.

Catalysis ability of the nanoreactor for glucose ex vivo

The nanoreactor can start to an acid-responsive catalytic cascade reaction, which can be self-sensed by the AgNPs@MBN element on the nanosensor. The sensing mechanism is as follows: a lower pH environment causes the damage of ZIF-8 cages,

making the leakage of GOx from the cages. In the appearance of glucose, the released GOx reacts with glucose to produce H_2O_2 and D-gluconic acid (Reaction 1). One of the catalysis products, H_2O_2, can induce a "turn-off" mechanism of the SERS intensity of the Raman reporter (MBN) laid on AgNPs due to the etching effect on AgNPs.

The SERS intensity of the AgNPs@MBN nanoprobes before and after the nanoreactors reacted with glucose was tracked, and the catalysis abilities under different pHs were compared by the changes of their SERS intensities. The prepared nanoreactor was centrifuged at 7000 rpm for 10 min and re-dispersed in PBS solutions with the pHs of 4.5 and 7.0, respectively. Then, a glucose solution (5 mM, 20 μL) was added into 200 μL of the nanoreactor solution (0.8 mg/mL) and the catalysis reaction between GOx and glucose was carried out in 37℃ for 3 h. Next, we dripped 10 μL of the resulting solution onto a glass slide for SERS measurements to trace the catalysis activity of GOx under an acid condition, and the results of which are shown in Figure 2a.

Next, we optimized the detection sensitivity of the nanoreactor *ex vivo*. In the assay, 200 μL of the nanoreactor PBS solution (0.8 mg/mL, pH=4.5) was mixed with 20 μL of different concentrations of glucose (0-10 mM) and the mixtures were incubated at 37℃ for 3 h. The SERS measurements are as same as described above and the results are presented in Figure 2b. We plotted the peak intensities at 2226 cm^{-1} with the glucose concentration and a linear fitting curve was obtained as shown in Figure 2b. It gives a fitting equation as $y=0.1605+0.0419\ x$, with a $R^2=0.9254$.

Cell culture

HeLa (cervical cancer cell line) and H8 (cervical epithelial immortalized cell line) cells were bought from the American Type Culture Collection (ATCC, USA). The two cell lines were cultured in the Dulbecco's Modified Eagle's Medium (DMEM) supplemented with 10% fetal bovine serum (FBS), 100 U/mL penicillin, and 100 μg/mL streptomycin at 37°C in a humidified atmosphere containing 5% CO_2.

Internalization of nanoreactors in cells

HeLa cells (or H8 cells) at a density of 1×10^5 cells per mL were planted into 35 mm culture dishes for 12 h, and then they were incubated with the nanoreactors (20 μL, 0.8 mg/mL) at 37 °C for 6 h (different culture time were also tried as 0, 2, 4 and 6 h). After that, the mediums were removed and the cells were gently washed three times with PBS.

Intracellular glucose determination by the nanoreactor

To confirm the glucose consumption in cells, the HeLa cells with nanoreactors in one dish were fixed by 4% formaldehyde every one hour, and totally, eight samples representing 0-7 h of the reaction time were achieved. The SERS spectra of the SERS nanoprobes on the endocytosed nanoreactors were recorded on the fixed cells, which can report the intracellular glucose amount during the different treatment stages, as shown in Figure 3d.

Rhodamine B-encapsulated ZIF-8 NPs for living cell imaging

To achieve the location information of the nanoreactors within cells, we prepared the RhB/ZIF-8 NPs and characterized them with a confocal laser scanning microscope (CLSM). In a typical preparation, 0.117 g of zinc nitrate was dissolved into 0.8 mL of DI water, while 0.1 mg of rhodamine B (RhB) was added into the zinc nitrate solution to stir at 30 ℃ for 10 min. Then, 2.27 g of 2-methylimidazole in 8 mL of DI water was added into the mixed solution under vigorous stirring for another 10 min. The resulting RhB-encapsulated ZIF-8 NPs were centrifuged at 8000 rpm for 10 min and washed with DI water.

The HeLa cells (1×10^5 cells/mL) were cultured with 0.8 mg/mL of the ZIF-8@RhB NPs. The internalization of the nanoreactors can be controlled by different incubation time (0, 2, 4 and 6 h). Subsequently, the cells were washed again by the cold PBS and then they were stained with LysoSensor™ Green (2.5 μg/mL) for 20 min. After three times washing, the cells were observed by the CLSM with a 40× objective.

Cell viability assay

The cell viability test was performed with the standardized MTT (3-(4, 5-dimethylthiazol-2-yl)-2, 5-diphenyltetrazolium bromide) assay. Typically, the cells were seeded on the 96-well microtiter plates for 12 h incubation at 37 ℃. Then, the cells were washed three times using the cold PBS. Different concentrations of ZIF-8@GOx-AgNPs@MBN NPs were added into each well, supplemented with the complete medium to 100 μL, and then they were cultured at 37 °C for another 24 h. After the cells were washed with the cold PBS, 5 μL of the MTT solution (5.0 mg/mL) was added into each well for additional 4 h at 37 ℃. Finally, after removing the medium, 150 μL of DMSO was added into each well to dissolve the purple formazan crystal. The absorbance of each well was measured at 570 nm by a microplate reader and the MTT results are shown in Figure S7a.

Also, we assessed the cell viabilities of HeLa cells by the MTT assay when the cells were cultured with Ag^{+}, Zn^{2+}, Ag^{+}/Zn^{2+}, with or without glucose (5 mM) for 24 h. The results are displayed in Figure 3e and 3f.

Live/dead cell staining

The cells (seeded density is 1×10^{5} cells/mL) were stained with calcein-AM (2 μM) and propidium iodide (PI, 4 μM) for 20 min. Finally, the stained cells were washed three times using the PBS and they were imaged by using a Leica DMI6000B microscope with a 10× objective (Figure 3c).

For a comparison, PBS (control), ZIF-8, ZIF-8@GOx (0.8 mg/mL), and AgNPs@MBN (2.5×10^{-5} M) were also used instead of the ZIF-8@GOx-AgNPs@MBN for assessing their therapeutic effects (Figure 3c).

Evaluation H_2O_2 content change within HeLa cells

RDPP $[Ru(dpp)_3]Cl_2$ as a hydrogen peroxide fluorescence-specific probe (Qi et al., 2019), with a concentration of 0.3 μM, was incubated with the nanoreactors internalized HeLa cells for 30 min. Finally, the cells were washed with PBS three

times and the hydrogen peroxide highlighted by RDPP in the cells was observed under a fluorescence microscope (Leica DMI6000B, Germany) with a 20× objective.

Cell apoptosis assay by flow cytometry

For apoptosis analysis by flow cytometry, the HeLa cells were seeded in the 6-well plates at a density of 1×10^5 cells/well and grown overnight in 5% CO_2 at 37 °C. The adherent cells were treated by the nanoreactors (20 μL per well, 0.08 mg/mL) at 37 °C for different time (0, 2, 4, 6, 8, and 10 h, respectively). The cells were collected by 4 min of cell dissociation and centrifugation (1500 rpm, 3 min) followed twice PBS washing. Then, 200 μL of the binding buffer was added to re-disperse the HeLa cells. Annexin-V-APC (5 μL) and 7-AAD (5.0 μL) were added and cultured for 30 min, which can stain the live and dead cells according to the instructions. Finally, the flow cytometer was operated to detect cell apoptosis after the treatments.

Bio-TEM imaging of cells

The HeLa cells were incubated with 0.08 mg/mL of the nanoreactor in a DMEM medium in 5% CO_2 at 37 °C for 6, 12, 24 h, respectively. Then, they were washed twice using cold PBS (pH = 7.4) and detached by incubation with 0.25% of trypsin. The cell suspension was centrifuged at 1500 rpm for 3 min. After removing the culture medium, the cells were washed twice with PBS. The cells were fixed by glutaraldehyde at 4 ℃. The sample was rinsed with PBS and dehydrated by a graded ethanol series. The samples were then embedded in EPOM812 and polymerized in the oven at 37 °C for 12 h, 45 °C for 12 h and 60 °C for 48 h. The fixed sample was cut into many ultrathin sections with approximately 70 nm in thickness by a diamond knife on a Leica UC6 ultramicrotome. The sample sections were transferred to the copper grids and imaged on a JEM-1230 transmission electron microscope.

Animal experiments

BALB/c nude mice (four weeks old, 18 ± 0.2 g, female) were purchased from Beijing

HFK Biotechnology Ltd. (Beijing, China). Animal care and handling procedures were in agreement with the guidelines of the Regional Ethics Committee for Animal Experiments.

Tumor models and *in vivo* chemo-starvation therapy

The 50 μL of cell contained PBS solution (5×10^6 cells/mL) was injected into each mouse subcutaneously. The mice were applied for further experiments when the tumor had grown to 8-10 mm in diameter. Then, the mice were divided into six groups at random for the treatments with the following nanomedicines: control (PBS), AgNPs@MBN, ZIF-8@GOx and the nanoreactor of different concentrations (50, 100, and 200 μg/mL, respectively), with three mice set as one group. Above nanomedicines were injected intravenously into the mice.

To monitor the therapeutic effects of different nanomedicines, we measured the tumor size by using the digital caliper in two dimensions to calculate the tumor volume according to the following equation: Tumor volume = $(\text{length}\times\text{width}^2)/2$. Meanwhile, the body weight changes of mice were recorded every day to estimate the efficacy of physical recovery. On the 14^{th} day, the tumors were weighed to assess the therapeutic efficacy of different experimental groups.

In vivo biocompatibility evaluation

For *in vivo* biosafety evaluation, female nude mice were separated into six groups (n = 6) randomly when they were four weeks old, and they were treated with the control, AgNPs@MBN, ZIF-8@GOx and the nanoreactor at different concentrations (50, 100, 200 μg/mL, respectively). After a 14-day period, all nude mice were dissected to collect their organs (tumor, heart, liver, spleen, lung, kidney and muscle). The organs were cut into thin slides and fixed by paraformaldehyde (4 wt%) for the hematoxylin and eosin (H&E) staining assay. The blood samples of each experimental group including the control group were collected at the same time. Then, we measured the trace elements in the blood samples, including Pb, Zn, Cu, Fe, Ca and Mg. The Zn^{2+}

and Ag^+ contents in the above major organs were analyzed by the ICP-MS (Figure 4h and 4i), which can reveal the metabolism ways of Zn^{2+} and Ag^+ *in vivo*.

In vivo SERS detection

The BALB/c mice were received 200 μg/mL of the nanoreactor per kg by intravenous injection when the tumor reached 8-10 mm in diameter. The mice with 24 h and 14 d post-injection were anesthetized and examined under a confocal Raman spectrometer with 20 mW laser power at 785 nm (Figure 5g). The laser beam was focused on the tumors or normal muscles with a focal distance of ~ 9 mm. Thus, SERS spectra were obtained in a completely noncontact and noninvasive manner.

Lysosome extraction of HeLa cells incubated with the nanoreactor

The lysosome extraction from HeLa cells was performed directly after the incubation with the nanoreactors for 6 h according to the protocol indicated in the lysosomal extraction kit. Briefly, cells (～1×10^6 cells/mL) were centrifugated at 500×g rpm for 5 min under 4 ℃ to remove the culture medium and washed using a cold PBS solution twice. After that, the cold extraction A of 400 μL was adding into the cells on the ice for 10 min and using the homogenizer for 20-40 cycles of homogenization. Then, the gradient centrifugation of the cells was carried out at 4 ℃(: 1000 rpm for 5 min, 3000 rpm for 10 min, 5000 rpm for 10 min, 20000-30000 rpm centrifugation, 20 min) and the supernatant was kept each time by transferring to a new cold tube, except the precipitates were kept for the last high-speed centrifugation. Then, 400 μL of the cold extraction B were added, then the mixture was centrifugated under 20000-30000 rpm for 20 min at 4 ℃ and the precipitates were the lysosomes with the nanoreactors.

References:

Agnihotri, S., Mukherji, S., and Mukherji, S. (2014). Size-controlled silver nanoparticles synthesized over the range 5-100 nm using the same protocol and

their antibacterial efficacy. RSC Adv. *4*, 3974–3983.

Pan, Y.C., Liu, Y.Y., Zeng, G.F., Zhao, L., and Lai, Z.P. (2011). Rapid synthesis of zeolitic imidazolate framework-8 (ZIF-8) nanocrystals in an aqueous system. Chem. Commun. *47*, 2071–2073.

Qi, G.H., Zhang, Y., Wang, J.F., Wang, D.D., Wang, B., Li, H.J., and Jin, Y.D. (2019). Smart plasmonic nanozyme enhances combined chemo-photothermal cancer therapy and reveals tryptophan metabolic apoptotic pathway. Anal. Chem. *91*, 12203–12211.